Tectonophysics 911 (2025) 230830

Contents lists available at ScienceDirect

Tectonophysics

journal homepage: www.elsevier.com/locate/tecto

Subsurface characterization of crystalline rocks at the Einstein Telescope candidate site (Italy): Insights from seismic tomography, geoelectrical and morphostructural analyses

F. Villani[a], S. Maraio[a,*], L. Improta[a], P.M. De Martini[a], D. Cavallaro[a], M. Firetto Carlino[a], C.A. Brunori[a], V. Longo[b], L. Casini[b,c], M.C. Caradonna[d], C. Zei[a], S. Rapisarda[a], G. Oggiano[b], C. Giunchi[a], G. Saccorotti[a], M. Coltelli[a], D. D'Urso[b,c], L. Naticchioni[e,a], F. Ricci[e,f], G. Schillaci[c], D. Cittadino[c], M. Marsella[g], Q. Napoleoni[g], C. Rossini[g], G.L. Cardello[b,c]

[a] Istituto Nazionale di Geofisica e Vulcanologia, Italy
[b] Department of Chemistry, Physics, Mathematics, and Natural Sciences, Sassari University, Via Piandanna, 4, 07100 Sassari, Italy
[c] Istituto Nazionale di Fisica Nucleare - Laboratori Nazionali del Sud, Catania 95125, Italy
[d] Department of Mathematics and Earth Sciences, University of Trieste, Italy
[e] Istituto Nazionale di Fisica Nucleare - Sezione di Roma, Roma 00185, Italy
[f] Department of Physics - Sapienza, University of Rome, 00185 Roma, Italy
[g] Department of Civil and Environmental Engineering (DICEA) - Sapienza, University of Rome, 00185 Roma, Italy

A R T I C L E I N F O

Keywords:
Seismic profiling
Refraction tomography
Electrical resistivity tomography
Crystalline basement
Fault zone
Einstein Telescope Project

A B S T R A C T

The Einstein Telescope (ET) will be the first European underground observatory of gravitational waves. The observatory's interferometric detectors will be housed in a large underground infrastructure,which necessitates a stable and quiet geological context. We present the results of a geognostic campaign conducted for the Italian candidate site in Sardinia, during which two ~270 m-deep boreholes were drilled in granites and orthogneiss at two sites that are possible locations of the ET infrastructure. We acquired high-resolution, dense seismic and electrical resistivity tomography (ERT) profiles to complement borehole data, constraining the thickness of the weathered layer and characterizing the rock properties in terms of intact versus fractured zones down to depths of 100–240 m. At depths >50 m, we observed high P-wave velocity (Vp ~ 5000–5500 m/s, while very high Vp (~6000 m/s) paired with very high resistivity (ρ > 1000 Ωm) was found at depths of 150–200 m, suggesting unfractured or weakly fractured rocks consistent with borehole logs and literature data on geophysical surveys on crystalline rocks. We recognized a couple of sub-vertical low-Vp (~4250–4500 m/s) and low-resistivity anomalies (ρ < 500 Ωm), up to ~15–35 m-wide, suggesting the occurrence of fracture zones with groundwater, matching the intersection with fault zones mapped at the surface. Comparison with co-located resistivity sections, downhole seismic surveys, well logs, and field-based structural and morphostructural analyses allowed us to attribute these anomalies to fault zones ~0.3–0.5 km-long that belong to an immature fault network with shallow water circulation. This methodological approach highlights the utility of tomographic techniques combined with structural investigations and represents a guideline that can be applied in similar contexts characterized by poorly fractured crystalline rocks.

1. Introduction

The physical characterization of crystalline basement rocks through shallow geophysical surveys and borehole geophysical logging, in particular using active-source seismic methods, is critical for mining, geothermal and nuclear waste disposal projects, as well as for the construction of underground infrastructures (Moon et al., 1993; Everett, 2013; Schmelzbach et al., 2007; Siren et al., 2015; Buske et al., 2016; Hedin et al., 2016; Place and Malehmir, 2016; Wenning et al., 2017; Ahmed et al., 2019; Zhang et al., 2020; Elger et al., 2021). In these applications, seismic methods can be combined with field geological surveys and other imaging techniques, like ground penetrating radar –

* Corresponding author.
E-mail address: stefano.maraio@ingv.it (S. Maraio).

https://doi.org/10.1016/j.tecto.2025.230830
Received 2 December 2024; Received in revised form 11 June 2025; Accepted 14 June 2025
Available online 19 June 2025

GPR (e.g., Doetsch et al., 2020; Duz et al., 2023), airborne magnetic and electromagnetic soundings (Nasuti et al., 2015; Shah and Crain, 2018; Kuang et al., 2022), and electrical resistivity tomography – ERT (e.g., Meju, 2005; Aizebeokhai et al., 2018; Sahoo et al., 2024, 2025; Srivastava et al., 2024; Yadav et al., 2024). ERT is suitable to provide high-resolution images of the very near surface, particularly in correspondence of fault zones (Giocoli et al., 2015; Park and Roberts, 2003; Unsworth et al., 1997; Bharti et al., 2023), and is applied successfully for accurate imaging of the weathered portions of crystalline rocks (e.g., Clair et al., 2015; Belle et al., 2019; Aning et al., 2019). Moreover, ERT lends itself to a comparison and integration with seismic tomography, since the elastic properties of the rocks (e.g., in terms of velocity of propagation of compressional P-waves - Vp), in most cases display a good correlation with the mean rock resistivity (ρ) and can be interpreted in terms of lithology and fracturing (e.g., Meju, 2005). For instance, the spatial density and opening of fracturing control the occurrence of drops in mean Vp and ρ with respect to the surrounding relatively intact rock mass: such anomalies in some cases are related to the presence of hydraulically conductive fractures (e.g., Podugu et al., 2023). In this sense, fault zones are mostly imaged as relatively narrow zones characterized by significant lowering of Vp and ρ, or a combination of both, compared to the host rock (e.g.; Park and Roberts, 2003; Nguyen et al., 2005; Martí et al., 2006; Belle et al., 2019).

In this paper, we present an interdisciplinary exploration of the Italian candidate site to host the Einstein Telescope (Punturo et al., 2010) – hereafter ET – the first European underground gravitational wave observatory (https://www.einstein-telescope.it/; ET design report update 2020, 2020). To detect these waves, ET requires a tectonically stable site characterized by rocks with high-quality mechanical properties and by a low level of natural and anthropogenic noise.

We report the results of a combined approach including active seismic and geoelectrical surveys performed on the crystalline rocks exposed in the candidate site located in eastern Sardinia (Italy; Fig. 1). This work follows the encouraging very low levels of seismic ambient noise measured at Sos Enattos (Fig. 1;b Naticchioni et al., 2014, 2021; Di Giovanni et al., 2020, 2023; Allocca et al., 2021) and the extremely low degree of seismicity of the region (Meletti et al., 2020). The foreseen machine should provide valuable information on new sources of gravitational waves, such as intermediate-mass black holes (Allocca et al., 2021). Ideally, the caverns and tunnels hosting the technological infrastucture of ET should be covered by a ~ 150 m-thick layer of rock to greatly reduce environmental noise. In this frame, our work might help us predict the types of rock underground, the degree of fracturing and the occurrence of possible fault zones.

The study area encompasses the region north of the dismissed mine of Sos Enattos (Fig. 1). It is made of crystalline rocks of Variscan age (approximately 360–300 Ma; Ma). Our high-resolution geophysical investigations were carried out in 2021 and consisted in the acquisition of refraction and downhole seismic data, complemented by ERT surveys, in the proximity of two drilling sites, located in two sites suitable to host part of the ET infrastructure.. The study also included geological, morphostructural and structural surveys focused on the characterization of the bedrock structure in terms of morphological lineaments, foliation, faults and fractures.

Specifically, our results furnish insights that can be applied to the ongoing follow up study of the drilling sites in terms of Vp and electrical resistivity down to 100–200 m depth, to define the extent and thickness of the weathered rock cap, to infer rock fracturing, and to identify and scale the size of possible fault zones hosting perched aquifers. More in general, this approach can be applied to the physical characterization of similar rock masses.

2. Study area and geological setting

2.1. Regional constraints and local geological, structural and time constraints

The study area (Figs. 1, 2) lies in the Variscan crystalline basement of north-east Sardinia (Fig. 1) on a wide plateau at 800–1000 m above sea level (a.s.l.). The main lithostratigraphic units are metasediments of unknown age and orthogneisses derived from calc-alkaline magmatic protoliths of Ordovician age (Ferrara et al., 1978; Oggiano and Di Pisa, 1992; Carmignani et al., 1994). The overall structure is affected by Variscan deformation and metamorphism, which decreases towards the south from upper amphibolite to greenschist facies. During the Carboniferous and Permian, metamorphic rocks were intruded by late Variscan granitoids (Fig. 1b) of the Corsica-Sardinia Batholith (Casini et al., 2012, 2015a, 2015b). Dykes with both acid and basic composition are widespread in the area (Fig. 1b). Furthermore, arenized bands of granitoids exposed at roadcuts display a thickness in the range of some tens of meters.

From north to south, the geological succession in the study area comprises the following units (Fig. 1b): granitoids of the Variscan batholith; gneiss and migmatites (with subordinate calc-silicate rocks) hosting amphibolite bodies; micascists and paragneisses, predominantly milonitic; Lodé-Mamone granodioritic orthogneisses and augen-gneiss; garnet-bearing micaschists and paragneisses; meta-sandstones (e.g., at the Sos Enattos mine). The aforementioned drilling sites are located in the batholith (P2 in Fig. 1b) and in the Lodé-Mamone Orthogneiss (P3), respectively. The syntectonic metamorphic events recorded by the garnet-bearing schists have been dated near Mamone by Di Vincenzo et al. (2004) to 340–315 Ma.

The granitic rocks are affected by acidic dykes whose age is not known, however field relationships indicate an upper Carboniferous - lower Permian emplacement (e.g., Sos Canales granitoid; Di Vincenzo et al., 1994). Larger granitoid intrusions, 310–290 Ma in age, occur on the plateau (e.g., Sos Canales granitoid; Di Vincenzo et al., 1994).

2.2. Borehole stratigraphy

The investigated areas are located at two sites proposed for the ET project (Naticchioni et al., 2021, 2024). Two boreholes, namely P2 and P3 (Fig. 1b, 2 and 3), were entirely drilled using a destructive method through crystalline rocks and reached the depth of 283 m (P2) and 263 m (P3), respectively (described in Harms et al., 2022; Naticchioni et al., 2024).

At site P2 (see also Fig. 5), the Sos Canales leucogranite crops out as rounded metric to decametric granitoid masses surrounded by sandy-silty soil and alluvial deposits. Borehole P2 went across the leucogranites (Fig. 5a), encountering several levels of arenized and weathered granitoids accompanied by fractured zones and a variable level of water content. The main rock-properties inferred from this drilling are described more in detail in Section 4.1. In the surroundings, the Sos Canales massif also comprises medium-grained granodiorites and leucogranites.

Medium-grained orthogneiss with a strongly foliated and granoblastic texture crop out at site P3 (Fig. 9). This unit shows frequent gabbro-dioritic inclusions parallel to the main foliation dipping to the south. Borehole P3 (Fig. 8) mostly drilled orthogneiss, which maintained a nearly constant ESE foliation gently dipping (about 30°) towards the SE.

In places a thin cover or sandy-gravelous units fill the depression in between rounded rocky bumps. In both sites, seasonal streams appear during the heaviest rainfalls.

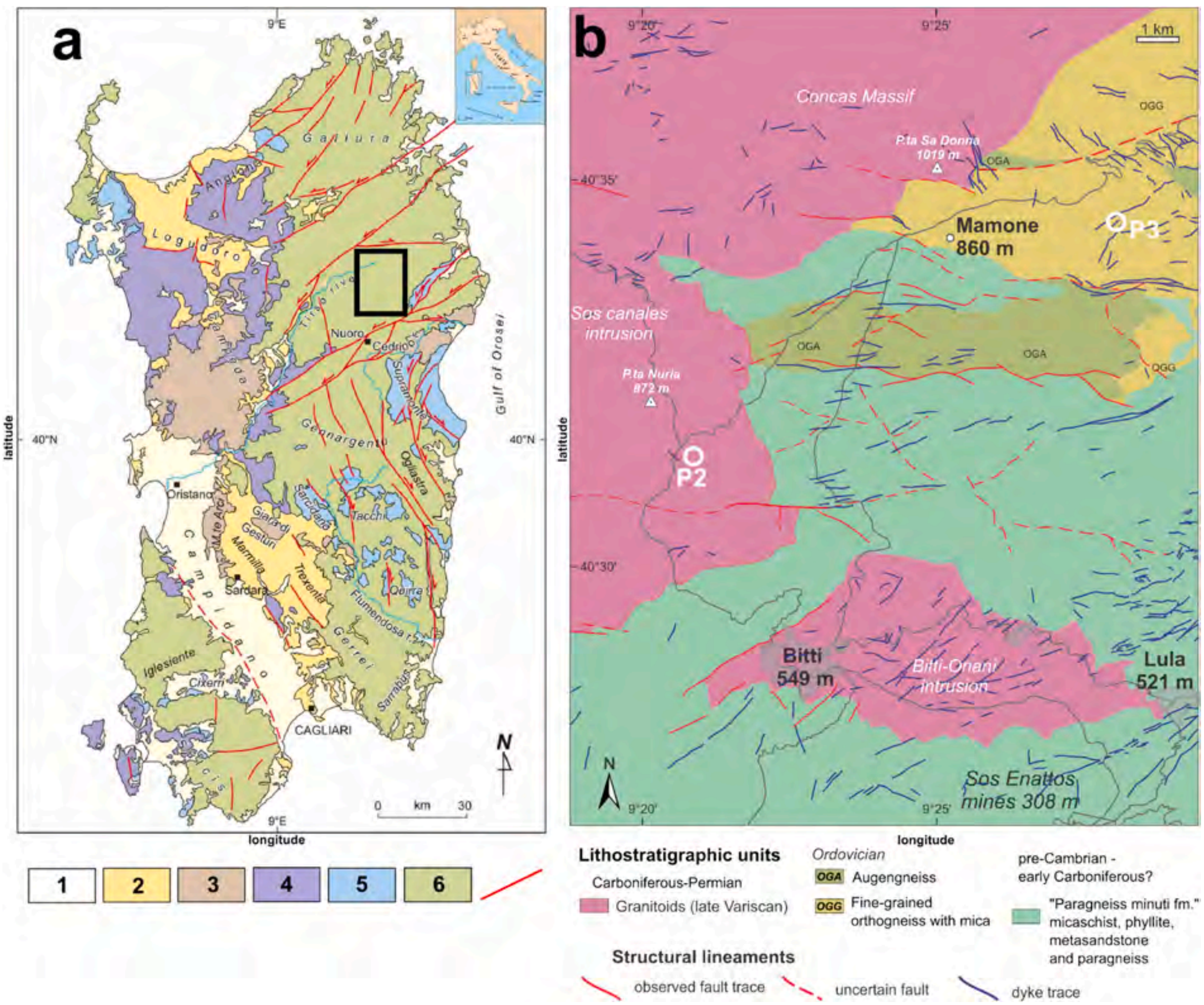

Fig. 1. a) Geological map of Sardinia (after: Carmignani et al., 2015). The black box indicates the study area with the candidate site for the ET infrastructure. Key to legend: 1) Quaternary deposits; 2) sedimentary rocks (upper Oligocene - Pliocene); 3) Basaltic lava flows (Pliocene-Pleistocene); 4) Volcanic rocks (Oligocene - Miocene); 5) Volcano-sedimentary rocks (upper Carboniferous - upper Eocene); 6) Variscan basement. Red lines are the major post Variscan faults. b) New detailed geological map with location of the sites of interest for the planned ET infrastructure: sites P2 and P3 are indicated with white circles. (For interpretation of the references to colour in this figure legend, the reader is referred to the web version of this article.)

3. Data and methods

The seismic surveys were carried out in both drilling sites by seeking the best compromise between the logistical and topographic conditions, yet with the aim of reaching an investigation depth comparable to that of the two drills.

The presence of several hundred meters thick crystalline rocks makes the study area difficult to investigate via multichannel reflection seismic techniques. Even in presence of fault zones, shallow reflection data acquired over crystalline rocks usually feature low signal-to-noise ratio and inconsistent reflection events (Kim et al., 1994; among others). For these reasons, the shallow imaging of fractured granites always requires developing target-specific and complicated data processing strategies (see Zhang et al., 2020), which do not ensure the achievement of satisfactory results.

For weakly fractured granitoids, as those of sites P2 and P3, the use of refraction seismic tomography and its integration with ERT is preferable for rock mass characterization (Martí et al., 2006; Clair et al., 2015). We used refraction tomography to reconstruct the spatial distribution of P-wave seismic velocity by means of inversion of traveltimes of direct waves, turning-waves and critically refracted waves. Our 2-D investigations were complemented by borehole downhole measurements involving 1-D traveltime tomography. We have also attempted to use multi-channel analysis of surface waves (MASW) for retrieving a shallow shear-wave velocity field (e.g., Park et al., 1999): however, our seismic data do not contain any significant Rayleigh wave energy.

We collected three high-resolution active seismic profiles using a multi-channel system involving 24-bit Geode© seismographs connected to up to 168 vertical geophones (4.5 Hz eigenfrequency). The main energizing system consisted of a 5455-kg high-frequency vibroseis (MiniVib from Industrial Vehicles International, Tulsa, Oklahoma, USA) that in favorable geological conditions allows an investigation depth of 500–1000 m. This source is very versatile, but it is not suitable for energizing on outcropping rocks and steep terrains. Unlike site P3, where we could acquire two seismic profiles with the vibroseis, at site P2 unfavorable geological and logistic conditions hampered its use. Here, we had to employ a minibang seismic gun, which is extremely versatile, although it allows a much shallower investigation depth (100–200 m).

A 14 Hz BHG-3 (GEOSTUFF - USA) borehole geophone was used for the acquisition of borehole seismics. The lower part of the probe contains a fluxgate-type compass, for orientation with magnetic north, and an amplifier to properly align the geophone components. The surface control unit employed for adjusting the anchorage and orientation is mod. BHGC-1 and a multicore with a Kevlar core, 250 m long.

The ERT surveys were carried out using a multi-electrode system (Dahlin, 1996) connected to Abem Terrameter LS2 device (ABEM

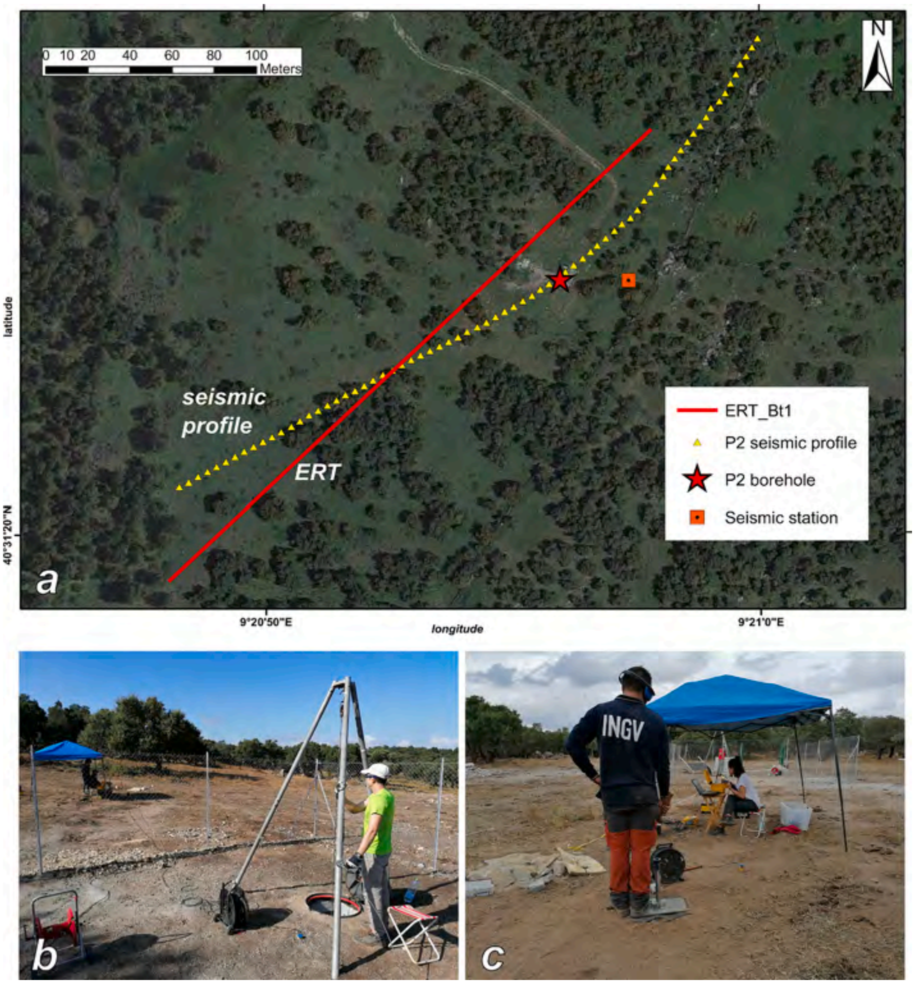

Fig. 2. Surveys at site P2 of the planned ET infrastructure and campaign activities. a) Outline of the seismic and electrical investigations carried out at site P2. The light blue line indicates the fence that hampered the acquisition of a longer seismic profile centered on the borehole. The location of the broadband seismic station is also shown (July 2021). b) Detail of the borehole with the sensor support tower during downhole acquisition. c) Detail of the acquisition system and the buffalo gun used for the energization (September 2021). (For interpretation of the references to colour in this figure legend, the reader is referred to the web version of this article.)

Instrument AB, Sweden). For each 2D electrical line, sixty-four electrodes were strung and anchored into the ground at a constant spacing (details in Table 2) and connected to a multicore cable (Longo and Cardello, 2021).

3.1. Seismic and electrical resistivity surveys: data acquisition and processing

The main characteristics of the acquired seismic and ERT profiles are reported in Table 1 and Table 2, respectively. The basic requirements for good data acquisition are slightly different for the two types of surveys. In the case of active seismics, the profiles were planned taking into account the presence of unpaved country roads, for the Minivib passage; this is also essential for a good coupling between the vibrator plate and the ground. Even if the seismic profiles are not perfectly straight, during the processing, we have applied crooked-line processing to overcome this issue. In the ERT acquisition, it is necessary to have the profile as straight as possible, avoiding areas of exposed rock, where electrode placement is impossible. In addition, for both acquisitions we had to plan the length of the surveys taking into account the eventual land-owners permits and the presence of "National" lands pertaining to the Mamone Prison, Italian Ministry of Justice, where any activity is hardly allowed. These are the main reasons for which the seismic and electrical profiles in sites P2 and P3 are not exactly coincident.

At Site P2 (Fig. 2), unfavorable logistical and geomorphological conditions influenced the design of the experiment. The position of the drilling site in the vicinity of high stone walls and fences, as well as the dense vegetation and a small granite ridge allowed collecting only one SW-NE oriented 360 m-long profile, which was tied to the borehole in the central part. The signals generated by 39 minibang gun shots were recorded by geophones spaced 5 m apart.

Concerning ERT, we acquired a 315 m-long profile with electrodes 5-m spaced (profile ERT_Bt1). This profile is nearly parallel and with the NE corner being shifted 65 m to the SW with respect to the seismic line. The array length and the consequent maximum investigation depth was limited by the site conditions, with dense vegetation and patchy outcropping rock.

We adopted Wenner-Schlumberger electrode configuration to guarantee proper investigation depth (about ⅙ of the overall profile length), and a good spatial resolution along vertical and horizontal directions. This is a good compromise for electrical imaging of complex structures, while allowing a good signal-to-noise ratio even on crystalline rocks (e.g., Bernardinetti et al., 2018). Due to the logistical issues mentioned above, it was not possible to exploit different array configurations or longer cables for the installation of remote poles.

For all ERT surveys, a delay time of 0.40 s and an acquisition time of 0.60 s were used. The delay time setting defines the interval between the switch-on of the current transmission and the start of signal integration

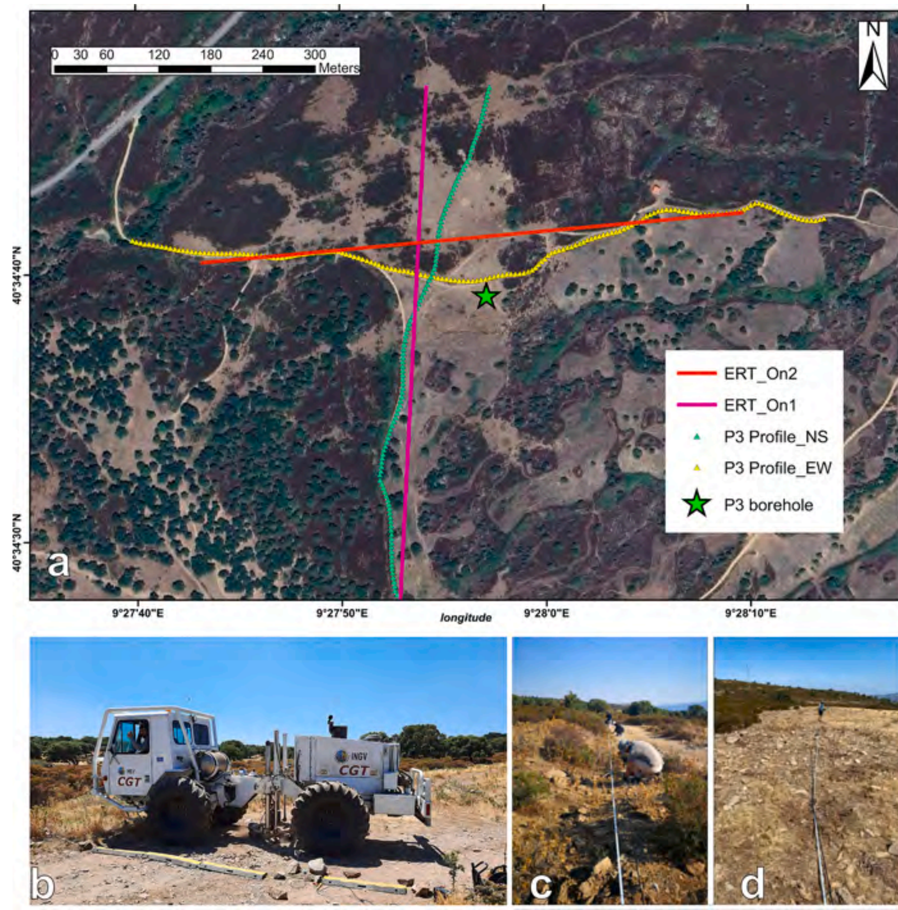

Fig. 3. Surveys at site P3 of the planned ET infrastructure and campaign activities. a) Acquisition plan, with location of the two orthogonal E-W and N-S seismic and ERT profiles (On1 and On2). The location of the P3 borehole is also shown. b) The MiniVib used for seismic data acquisition on profiles P3 E-W and N-S; c and d) deployment of electrode arrays for acquisition of ERT profiles On1 and On2.

Table 1
Details of the seismic profiles and downhole surveys.

Profile name	Length (m)	Number of geophones	Geophone spacing (m)	Number of shots	Shot spacing (m)	Traveltime readings for tomography	RMS tomographic model (sec)
P2	360	72	5	39	10	2520	0.00129
P2 downhole	234		2–4	100			
P3 N-S	720	144	5	69	10	7994	0.0023
P3 E-W (shallow)	840	168	5	79	10	9539	0.0021
P3 E-W (deep)	840	266	5			9712	0.13

Table 2
Details of the ERT profiles.

Profile name	Length (m)	Number of electrodes	Electrode spacing	RMS final model (%)
Bt1	315	64	5	8.4
On1	630	64	10	8.4
On2	630	64	10	6.8

for the resistivity measurement. Ideally, the delay time should be long enough to allow the ground to fully charge. If set to a short value, the effect of ground charge-up can cause a reduction in data quality. The acquisition time defines the duration of signal integration for each part of the measurement cycle. In general, the principle is that the longer the acquisition time, the better the data quality. During the measurement acquisition phase, a minimum and maximum current value of 0.0001 A and 0.2 A respectively was set, and stacking for a single measurement ranged from 2 to 4.

At site P2, a downhole survey was carried out, using the three-component borehole sensor described in Section 3.1. The acquisition procedure requires the energization to be close to the well mouth. A distance of 20 m was used for the investigation and the recording was made at depth intervals of 2–4 m for each shot (Fig. 2b, c). Seismic acquisitions were carried out from a depth of 234 m below ground level (b.g.l.) for a total of 100 shots by using the minibang seismic source.

At the P3 drilling site (Fig. 3), the suitable local logistic conditions allowed the acquisition of two long and almost orthogonal seismic profiles, which intersect 65 m from the borehole. Both profiles largely followed dirt roads, which represented an optimal condition for the coupling between the MiniVib source plate and the ground. The N-S oriented and 720 m-long profile (labeled P3 N-S) was acquired using 144 sensors spaced 5 m apart and 69 energization points (average spacing of 10 m). The *E*-W oriented and 840 m-long profile (labeled P3 E-W) was acquired using 168 vertical sensors spaced 5 m apart and 79 energization points (average spacing 10 m).

At each source position we recorded two, 5–200 Hz, 14.4 s-long linear sweeps from MiniVib. The receiver array record length was set to 16 s, with a sampling rate of 1 ms. These settings allow obtaining traces of 1.6 s length after correlation with the pilot trace. Source move-up was on average 10 m (Table 1).

The used acquisition geometry, namely dense wide-aperture seismic profiling (Ravaut et al., 2004; Bruno et al., 2017, 2022; Improta and Bruno, 2007), allows collecting simultaneously: 1) near-vertical and wide-angle reflections generated from deeper interfaces, the last being hardly detectable with shorter geophone spreads, and 2) highly redundant first P-pulses corresponding to shallow direct waves, deep-penetrating turning waves and critical refractions from the basin interior and its substratum, suitable for first-arrival traveltime tomography (Improta and Bruno, 2007).

The seismic profile P3 *E*-W is tied to the borehole, being the closest geophone located 15 m from the well. This made it possible to supplement surface data acquisition with simultaneous borehole measurements, improving depth sampling. We first placed the borehole geophone at 150 m depth to record 55 energizations spanning nearly the whole offset range (shot positions from 57.5 m to 837.5 m with average spacing of 10–20 m). Then, the geophone was put at 230 m depth, recording 22 energizations in a more limited offset range with shot positions from 7.5 m to 427.5 m and with average spacing of 10–20 m. Following the acquisition of the P3 E-W profile, we performed the downhole seismic survey in borehole P3. In this case, the MiniVib source was fixed 15 m from the borehole and energizations were recorded at regular intervals of 2 m, from 240 m to 24 m depth.

In site P3, two 630 m-long ERT profiles were also acquired, nearly parallel to the seismic profiles, with electrodes 10-m spaced (ERT_On1 and ERT_On2, respectively; Fig. 3a).

For all seismic profiles we hand-picked first-arrival traveltimes in the whole offset range. The travel times were inverted through a multi-scale non-linear tomographic technique based on a finite-difference eikonal solver (Podvin and Lecomte, 1991). This code (available at https://github.com/andherit/invdfe) was developed by Herrero et al. (1999) and validated through blind tests using seismic data and well logs acquired by oil companies (Improta et al., 2002). The tomographic technique combines the multiscale imaging strategy with a mixed global-local exploration of the model space, without requiring an initial reference velocity model. The 2-D Vp models are parametrized through a regular grid of velocity nodes. The multi-scale approach consists in gradually increasing the number of nodes during con*se*cutive inversion steps, resulting in an ensemble of models characterized by increasing spatial resolution, achieved at the expense of a loss in resolution depth. Models obtained at intermediate steps of the multi-scale inversion enable the reconstruction of large-scale and deeper velocity structures, while models obtained at late steps provide higher resolution images of the shallow subsurface. This tomographic technique is effective in the imaging of complex and heterogeneous structures, such as thrust-belts (Improta et al., 2002), continental tectonic basins (Improta et al., 2010; Villani et al., 2021), and shallow fault-zones (Villani et al., 2015; Maraio et al., 2023).

Model resolution is assessed through checkerboard sensitivity tests. We used smooth and small-amplitude checkerboard velocity perturbations to the best-fit models (values ranging from −20/+20 m/s to −50/+50 m/s) and then we repeated the inversion runs by using the perturbed synthetic traveltimes (see Improta et al., 2002 for more details). We show the results of resolution tests performed on models with different parameterizations in the Supporting Information: 1) coarse Vp-model with intermediate number of parameters, focusing on the large-scale structure of the subsurface; 2) models with a higher number of parameters, focused on the shallower features. Further details are in Section 4 and Supporting Information Fig.s S2-S7.

For the computation of the 1-D velocity model from the downhole data recorded in the P2 borehole, we used a different inversion scheme (Rayfract© code), based on the wavepath eikonal tomography (WET, Schuster and Quintus-Bosz, 1993; Lecomte et al., 2000; Watanabe et al., 1999). WET is based on the backprojection of traveltime residuals along wavepaths from the receivers to the source. Thickness of wavepaths depends on the bandwidth of the seismic signal. Picked first-arrival traveltimes are inverted within an initial smooth slowness model, and the eikonal equation is efficiently solved by a finite-difference method computing traveltime residuals. The slowness model is updated and these steps are iteratively repeated until convergence.

Worthy to note, we tried to exploit reflections from the acquired seismic dataset. We anticipate that, as expected for thick and massive granitoid and orthogneiss as those drilled in sites P2 and P3 (see more details Sections 4.1 and 4.2), a careful inspection of common shot gathers and velocity analyses did not reveal any clear reflection hyperbola, so that no input data could be provided for stacking and workflow of reflection processing.

Concerning ERT data, the processing workflow consisted in filtering and despiking of noisy data as derived from very low voltage and/or injected current in the ground. In general, data quality is very high, and thus only few measurements were culled from each ERT dataset. Despiked and filtered raw apparent resistivity data were input to a 2-D regularized least squares inversion algorithm with smoothness constraints (Loke and Barker, 1995; Constable et al., 1987; Loke and Dahlin, 2002). All 2D apparent resistivity data were inverted using the Res2Dinv inversion software (Loke, 2010). The forward problem was solved using the finite-element method (Silvester and Ferrari, 1996), in which node positions were adjusted to allow for topography to be taken into account during the inversion process (Loke, 2010). The standard Gauss–Newton optimization method was used, with a convergence limit of 0.005, and the Jacobian matrix was recalculated for the first two iterations. A higher-resolution model, with a cell width of half the minimum electrode spacing, was employed.

The inversion scheme converged quickly after a few iterations due to the high-quality of data. The output resistivity model is described in terms of the percent root mean square (% RMS) of error of a L2-norm misfit function.

3.2. Field structural survey and morphostructural analysis using satellite images

Foliation attitudes were extracted from published maps within the study area (Servizio Geologico d'Italia, 1962; Carosi et al., 2020; https://www.sardegnageoportale.it/) and also acquired in the field. To elucidate fault kinematics, a structural field survey was conducted, capturing measurements of folds, faults, fractures, and slicken-fibers at key locations. These data were processed using TectonicsFP (Ortner et al., 2002) and Stereonet software (Allmendinger et al., 2012) employing lower hemisphere projections and rose diagrams for visualization. Specifically, at each locality, eigenvectors were computed from bedding data, providing insights into the orientation of deformation axes.

Morphostructural lineament maps for the two drilling areas P2 and P3 were generated using satellite images from Google Earth Pro, allowing for local control over digitized structures (see Figs. 10, 11). The sampled areas represent the geological formations intersected by the boreholes at Onanì and Bitti, characterized by the presence of high-angle faults. Utilizing the FracPaQ toolbox (Healy et al., 2017), a multiscale analysis of fracturing was conducted on Variscan crystalline rocks such as those drilled in the study area. The multiscale combined field survey of morphostructures from Digital Elevation Model (DEM) (from https://www.sardegnageoportale.it/), satellite image analysis and fault segments from field mapping (see Fig. 1b) enabled a geometrical comparison of principal fault segments, encompassing trace length and orientation (section 4.3) and their relationships with the Vp and resistivity models recovered in the surroundings of the two boreholes P2 and P3.

3.3. Borehole logging

For the interpretation of our geophysical and geological dataset, we use fracture logging and resistivity measurements performed into boreholes P2 and P3 (preliminary results shown in Harms et al., 2022; Naticchioni et al., 2024). In particular, fracture logging was carried out with an OBI (Optical Borehole Imaging) probe equipped with a 1/3-in. high-resolution CMOS digital photo sensor. The orientation of the images obtained, along with the azimuth and inclination of the borehole were obtained with a 3-axis fluxgate magnetometer and 3 accelerometers. This kind of analysis was paired with the use of an ALT - QL40 CAL three-arm caliper (40 mm diameter), which provided the diameter of the borehole with a sampling of 5 cm, useful for the determination of fracture aperture, an important parameter that can be related to the mean physical properties of the rock mass.

Resistivity measurements were done using ALT – QL40 ELOG probe, with a sampling interval of 5 cm. The obtained values are representative of a limited volume in the surroundings of the borehole. The results are described in Section 4 in parallel with the results of seismic and electrical resistivity tomography.

4. Results

4.1. Results from geophysical investigations at site P2

The multi-scale refraction tomography was performed by modeling 2520 first arrival traveltimes (RMS of picking uncertainty: 1.26 ms). The final model (Fig. 4a), defined by 345 parameters, has a depth of investigation of approximately 90 m. The checkerboard resolution test performed on a model with an intermediate number of parameters (126 nodes, Fig. S3) shows that the central-eastern part of the model is resolved down to a depth of 60–80 m, while the western part is resolved down to a depth of about 50 m.

In Fig. 4a we see that the top low-velocity layer is thin (< 20 m) and characterized by Vp rapidly increasing with depth from 1500 to 2000 m/s to 4000 m/s. Two remarkable high-Vp regions are present on both sides. Vp > 5000 m/s is retrieved at only 20 m depth below the surface on the western side and at about 30 m depth to the east. The two high-Vp regions merge into a zone of extremely high-Vp (Vp around 5500 m/s) at the model bottom. A sub-vertical, low-Vp anomaly is observed in the central part of the model (x = 170–200 m) between 15 and 60 m b.g.l.. This structure is 15–35 m wide and characterized by a drop in Vp from 4750 to 5000 m/s to 4000–4250 m/s.

For ERT profile Bt1 (Fig. 4b), the best-fit resistivity model was achieved after 3 inversions with a RMS error of 8.4 %. Although the ERT does not cover the whole length of the seismic profile, it shows features that are in accordance with the Vp images. High-resistive rocks (ρ > 700–1000 Ωm) underneath a thin top layer of relatively low resistivity (ρ < 500 Ωm) are found. A wide relatively low-resistivity region (ρ ~350–500 Ωm) appears in the central part of the section, at depths of 25–50 m. This anomaly partly correlates with the low-Vp zone in the 2-D Vp model, although they do not perfectly match (Fig. 4) because the seismic and ERT profiles are not exactly co-linear (see Fig. 2).

The stratigraphy of borehole P2 (Fig. 5a) is compared with the Vp model obtained from a tomographic inversion of the picked arrival times for the down-hole survey (by using Rayfract© code) (Fig. 5b) and with the corresponding Vp vertical profile (Fig. 5d). The seismic ray coverage (Fig. 5c) decreases with depth, reaching low values for depths >150 m b.g.l.. Therefore, we consider the well-resolved portion of the profile to be approximately 150 m-deep. The P2 downhole model shows velocities

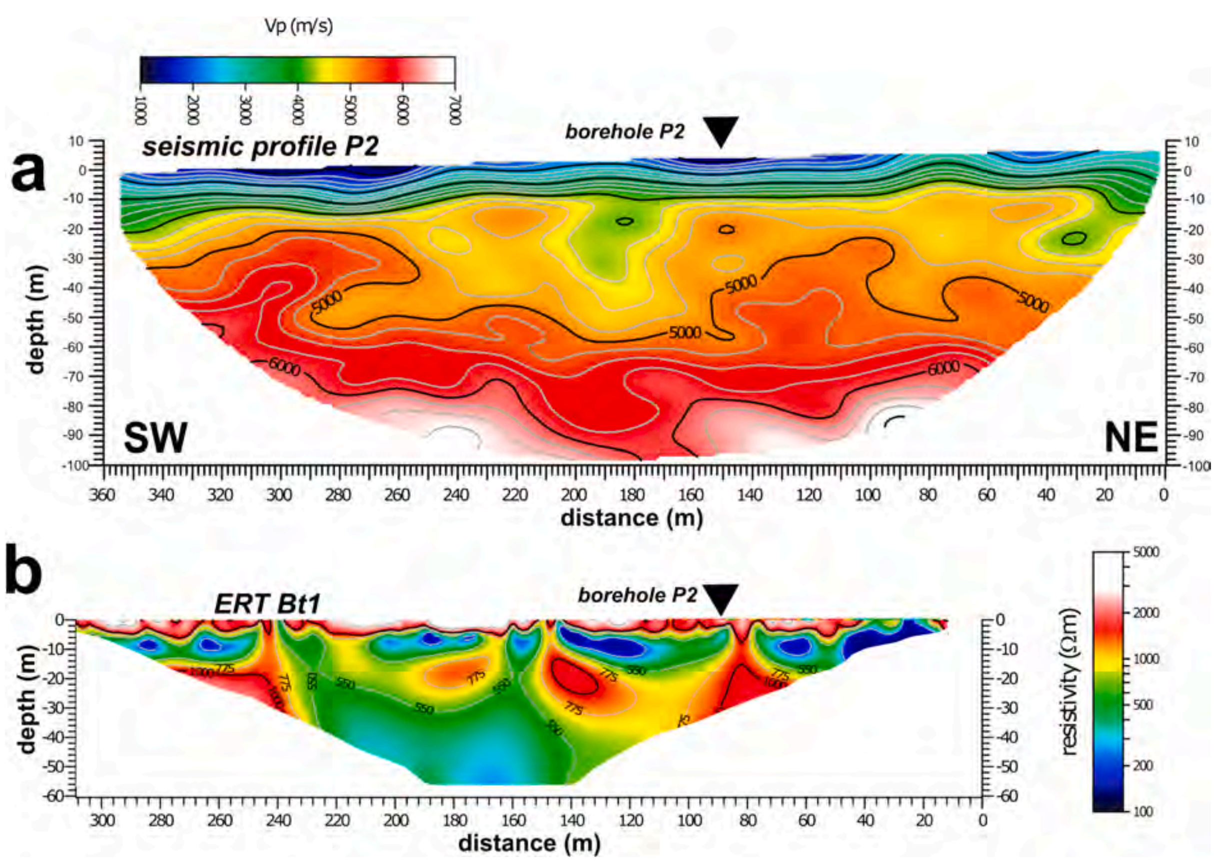

Fig. 4. Geophysical prospecting at site P2. a) Vp velocity model obtained inverting 345 parameters (spacing of velocity nodes: 16 m in x and 8 m in z). The velocity model is cut according to the ray coverage (Fig. S3). b) Results of the ERT survey Bt1 (projected onto the seismic profile). The black triangle indicates the projected location of borehole P2 on the seismic and ERT sections. Note that since the two profiles are not exactly collinear and have a different origin, the distances on the X axis are measured from each NE vertex of the seismic tomographic model and the ERT, respectively.

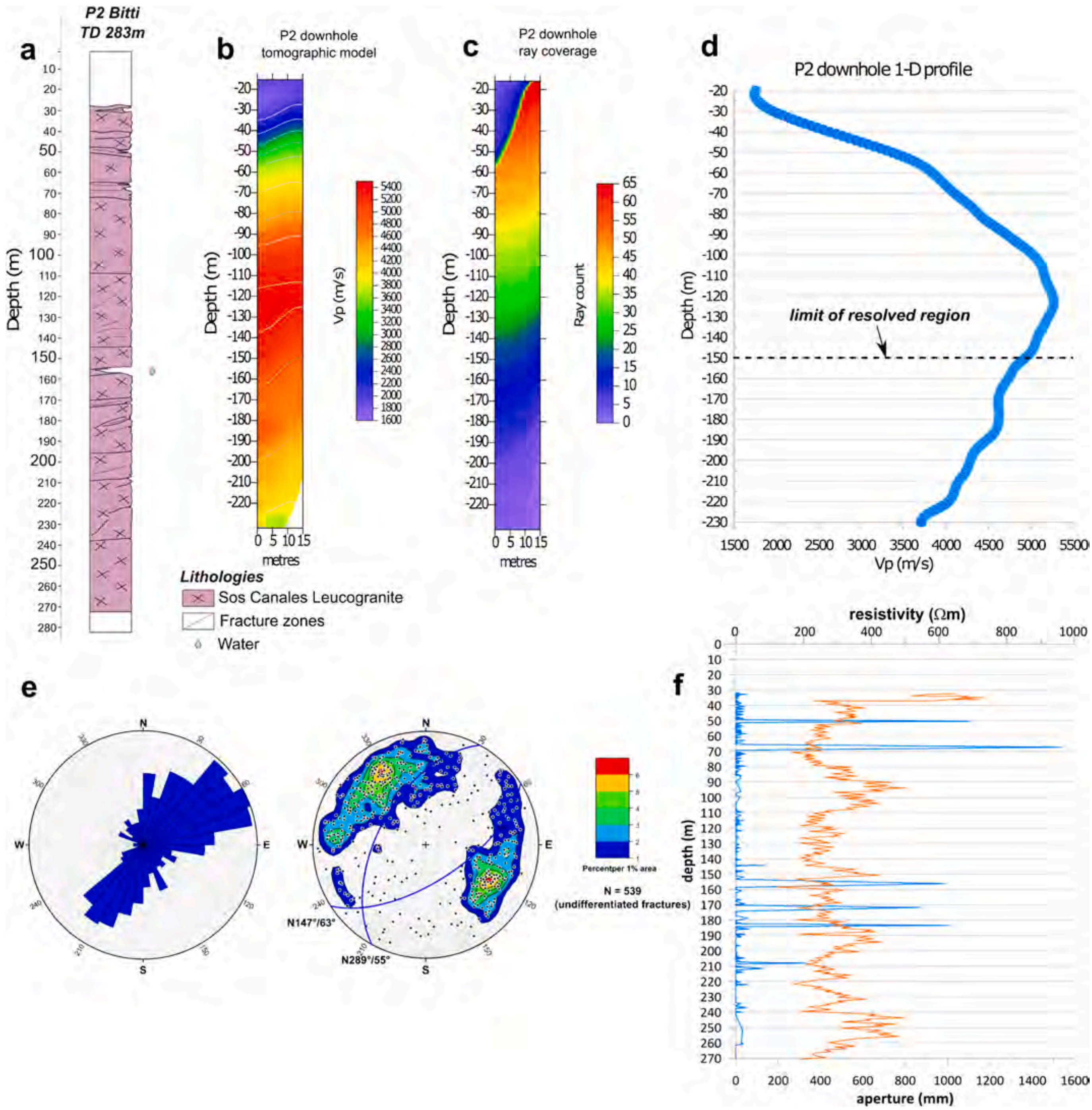

Fig. 5. Results of geophysical surveys at borehole P2 Bitti. a) stratigraphy; b) tomographic velocity model; c) ray coverage plot (i.e. number of rays per unit cell in the tomogram); d) 1-D velocity profile obtained from the tomographic inversion of downhole data; e) rose diagram of fracture azimuth and stereoplot of the poles to fracture planes collected by means of borehole optical imaging (two main sets are recognized, one with average attitude N289°/55° and the other one with average attitude N147°/63°); f) fracture aperture from caliper logging (blue curve) and resistivity log (orange curve) along borehole P2. (For interpretation of the references to colour in this figure legend, the reader is referred to the web version of this article.)

that rapidly increase with depth from 2000 to 5500 m/s.

The down-hole seismic survey (Fig. 5d) defines three zones: 1) strong Vp gradient (from 2000 to 4000 m/s) in the first 40 m; 2) significant Vp increase (up to about 5500 m/s) down to 100 m depth; 3) from 100 to 150 m depth low Vp changes (in the range 5000–5500 m/s). The quantitative comparison of the velocity values of the down-hole survey and refraction tomography is not feasible, since the former is characterized by prevailing vertical ray paths, whereas the deep portion of the tomographic model is mainly sampled by refracted waves with dominant horizontal propagation. Moreover, the two methods have different spatial resolution. Here, we remark that the two surveys define a similar velocity trend, having a steep velocity gradient in the shallowest portion and very-high Vp (around 5000–5500 m/s) in the deep part. This trend, together with the observed very-high Vp values, indicates a rapid transition from altered to unweathered granite (within the topmost 30–50 m; e.g., Flinchum et al., 2018), also suggesting a rapid closure of fractures with increasing confining pressure (Clair et al., 2015).

Structural data collected within the borehole P2 Bitti are reported in Fig. 5e as undifferentiated fractures. The rose diagram as well as the contour diagram of the poles to the fractures show that two main sets of fractures can be recognized. In particular, one set has an average dip 289°/55° (corresponding to a peak directional class of N040°-060° in the rose diagram), and the other one average dip 147°/63° (corresponding to a peak directional class of N210°-220° in the rose diagram).

The average fracture density (expressed as number of fractures per meter) in granites within borehole P2 is $2.25 \pm 2.03\ m^{-1}$ (Fig. S8a) and occurs with a slight trend of density reduction as a function of the depth, from 6 to 10 m^{-1} to 1–5 m^{-1}. An additional important parameter is fracture aperture, which was measured with the caliper starting from a depth of 30 m (the first 30 m of the borehole are cased and measurements in this range are discarded; Fig. 5f). The results show that granites have a low degree of fracturing along almost the entire length of the borehole P2. Six thin intervals with significant fracture opening (> 300 mm) were found at depths of about 50, 70, 155, 175, 185 and 210 m depth, respectively. The largest opening is found at about 70 m depth, and corresponds to a depth with a significant drop in resistivity (ρ 200–300 Ωm) (Fig. 5f) and groundwater circulation (Fig. 5a). The region with highest density of open fractures is found at 150–190 m depth: such depth intervals also correspond to relatively low resistivity values (ρ ~300 Ωm; Fig. 5f). This setting indicates that granites with low background fracture density may be affected by localized bands of more intense fracturing.

We point out that the small size of low-angle dipping fractures, which likely represent the only potential reflective seismic interface (Fig. 5e), may explain the lack of reflected events in our 2-D seismic dataset. This is the reason why we do not show the results of reflection processing.

4.2. Results from geophysical investigations at site P3

The seismic tomography and ERT results are described starting from profile P3 N-S (Fig. 6). The multiscale seismic tomography was performed by inverting 7994 first arrival traveltimes (RMS of picking uncertainty: 2.23 msec) read up to a maximum source-receiver distance of 715 m. Both seismic profiles are not perfectly rectilinear, so we used a crooked-line pre-processing workflow to discard seismic traces affected by 3D effects.

The ray density plot shows a maximum investigation depth of 110–120 m, but refracted waves are mostly confined in the uppermost 80 m (Fig. S4). The result of the resolution tests (performed on a model with an intermediate number of parameters, $N = 240$; Fig. S4) confirms that the resolution depth is about 80 m in the central-southern part of the model, while it is 40 m in the northern part. The velocity structure is characterized by extremely fast lithologies (Vp > 5000 m/s) from 30 to 40 m depth downwards. This explains the relatively shallow propagation of the refracted waves.

For ERT profile On2 (Fig. 6b), the best-fit model was achieved after 3 inversions with a RMS error of 6.8 %.

The velocity and resistivity models are consistent, with high Vp regions that spatially correlate with high resistivity and *viceversa* (Fig. 6a-b). The top low-velocity layer (Vp < 3000 m/s) get thinner from the southern end of the profile to x ~ 340 m, which agrees with high-resistivity in the near surface (ρ > 1000 Ωm). The region of extremely-high velocity (Vp > 5500 m/s with isolated spots of 6000 m/s) imaged at 40–50 m depth in the central-southern part relates to extremely-high resistivity values (ρ 2000–3000 Ωm). At the northern edge of the ERT model, we observe an abrupt lateral change in resistivity at x = 500 m (ρ decreasing from 2500 to 600 Ωm), associated with a small wedge of low-resistivity down to 50 m depth. This feature might be related to a small, wedge-shaped anomaly with relatively low-Vp (about 3500 m/s) in the velocity model. In this case, caution is needed in jointly interpreting the model features for two reasons. First, the low-resistivity anomaly is located at the edge of the ERT profile, where the investigation depth and resolution is lower. Then, in the northern sector, the ERT and seismic profiles are up to 60 m apart (Fig. 3a) and this hampers the

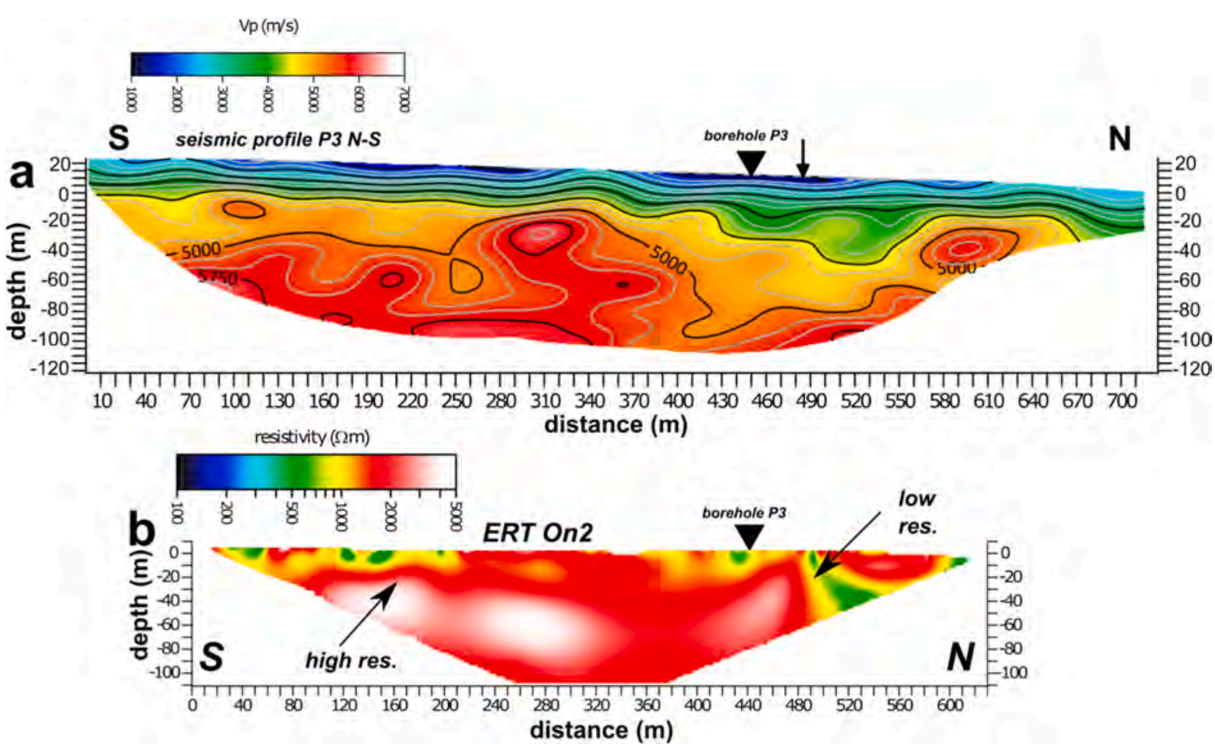

Fig. 6. Geophysical prospecting at site P3, transect N-S. Please note that depth is referred to the lowest point along the seismic profile. a) Vp tomographic model for profile P3 N-S obtained by inverting 360 parameters (velocity node spacing: 34 m in x and 13 m in z). The Vp model is cut according to the ray coverage (see Fig. S4). The black arrow indicates the intersection with the *E*-W profile and the black triangle represents the projection of the borehole P3 position on the seismic profile. b) ERT model On2.

direct comparison of the two observed anomalies.

Fig. 7 shows the results of the geophysical surveys along transect P3 E-W.

The tomographic model was obtained integrating traveltimes read from surface geophones with those from borehole measurements. The dataset from surface geophones consists of 9539 first arrival times (RMS picking uncertainty 2.34 msec). The maximum reading distance is 725 m due to the crooked geometry of the profile. The borehole data include traveltimes picked for a geophone placed in the borehole at 150 m and 230 m depth during the surface survey (77 arrival times), and traveltimes of the downhole survey (94 arrival times). The inversion of both surface and borehole data allows reaching a maximum investigation depth of about 240 m b.g.l. in the central part of the profile. Fig.s S6 and S7 show the results of the resolution test together with the ray density plot. Ray coverage is quite asymmetric in the deep part, due to the fact that the geophone placed at 230 m depth into the borehole recorded shots located only in the first half of the profile (see details in Section 3.1). The model is resolved down to depths of 170–220 m b.g.l. on the western-central portion (corresponding to −110/−170 m in Fig. 7a) and to depths of 70–90 m b.g.l. on the eastern edge (corresponding −50 m in Fig. 7a). The shallow model obtained only with surface seismic data is shown in Fig. S5. It is resolved down to about 60 m depth on the western side, 100 m in the central part, and 60–80 m on the eastern side. Thus, borehole seismic data allowed significantly increasing the resolution depth below the western-central part of the seismic line. We note that the two models have a very similar velocity distribution in the shallow part.

The top low-velocity layer of weathered rocks (Vp 1500–4000 m/s) is only 20–30 m thick (Fig. 7a), similarly to what is found at site P2. Below this shallow layer, velocities are very high and increase with depth from 5000 to 6000 m/s. Very-high Vp around 6000 m/s are retrieved at 90–100 m depth b.g.l. on both model sides and at about 160–170 m in the central part. Slightly lower velocities (Vp 4500–5000 m/s) characterize a small region at x = 320–400 and 70–80 m depth b.g.l. located a few meters to the west of the borehole.

For ERT survey On1 (Fig. 7b), the best-fit resistivity model was achieved after 5 inversions with a RMS error of 8.4 %. We found a general agreement between the resistivity and velocity distribution. The retrieved very-high resistivity (ρ 1500–3000 Ωm) is coherent with the presence of very-high Vp rocks (> 5000 m/s). Spots of relatively low-resistivity (ρ 200–600 Ωm) are present only in the near-surface, corresponding to the top low-velocity layer. A small region with a slight reduction of resistivity from ρ 1200 to 2000 Ωm is defined at x = 350–430 m at about 70 m depth, which roughly matches the region with low vertical Vp-gradient (4700–5000 m/s) in the tomographic model (Fig. 7a) at comparable depths.

As stated above, in the drilling site P3 (stratigraphy reported in Fig. 8a), the use of additional borehole seismic data allowed a good ray coverage together with a near-vertical propagation. Therefore, we extracted from the 2-D model a 10-m thick slice in correspondence of the borehole to illustrate the vertical velocity structure and ray sampling (Fig. 8b and c). Fig. 8d displays the vertical velocity profile calculated by horizontally averaging values of the Vp slice. The first 30 m show a step velocity gradient as a function of depth, with Vp increasing from 1500 m/s to 4000 m/s. From 30 to 75 m depth, the Vp gradient is lower and the velocity increases up to 5300 m/s. A main velocity reversal is defined below 75 m depth, with Vp decreasing down to 5000 m/s. Then the velocity increases again from 5000 to 5600 m/s between 95 and 130 m depth, and to 6000 m/s around 170 m depth. Very-high Vp values (5800–6000 m/s) persist down to the limit of the resolved region (about 220–230 m depth; Fig. S6 and S7).

The structural data collected in the borehole P3 revealed two main types of fractures. The first type is roughly parallel to the main foliation (Fig. 8e). The second type cross-cuts the foliation (Fig. 8f). Two main directional trends of fractures are evident. The first one is NE-striking, with a dominant strike N040°-050° related to the main foliation, and to a

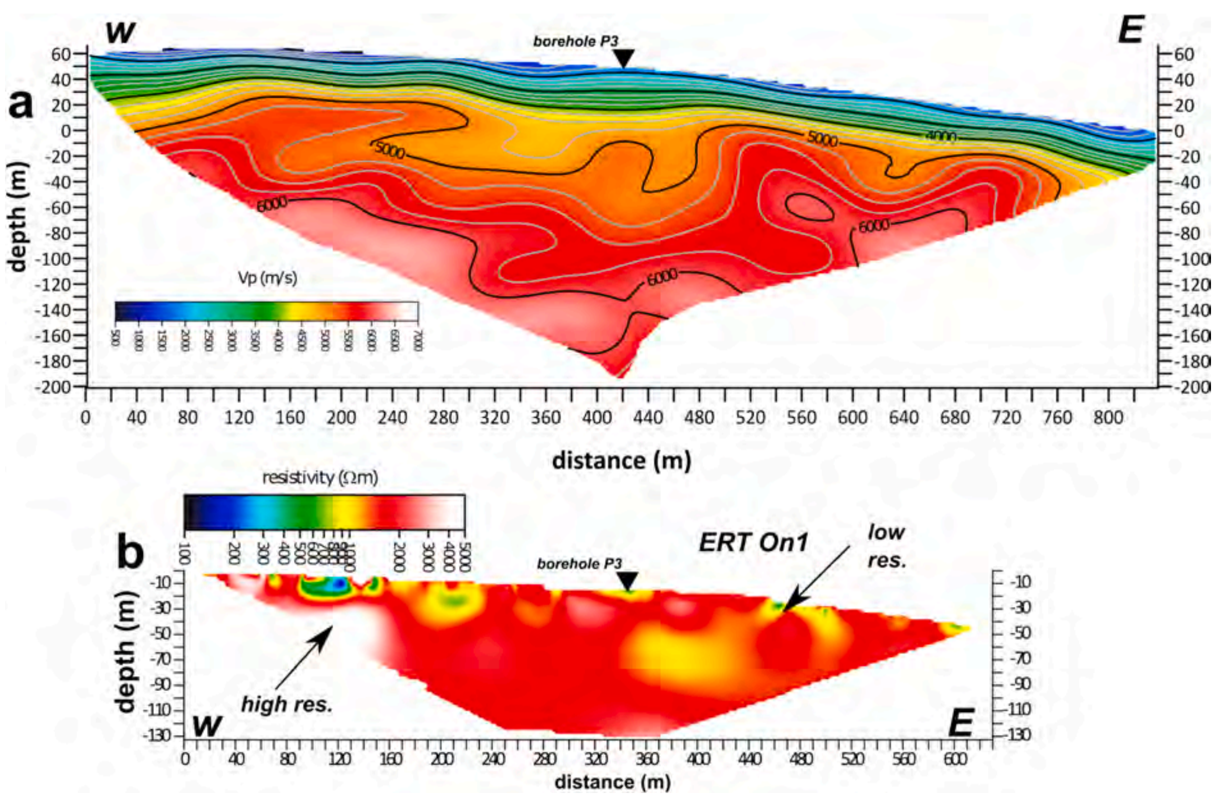

Fig. 7. Geophysical prospecting at site P3, transect E-W. Please note that depth is referred to the lowest point along the seismic profile. a) Tomographic Vp deep model obtained using both surface and downhole seismic data (the model is cut according to ray coverage: see Fig. S6, S7); this model was obtained by inverting 209 parameters (velocity node spacing: 49 m in x and 25 m in z). b) Co-located ERT model On1.

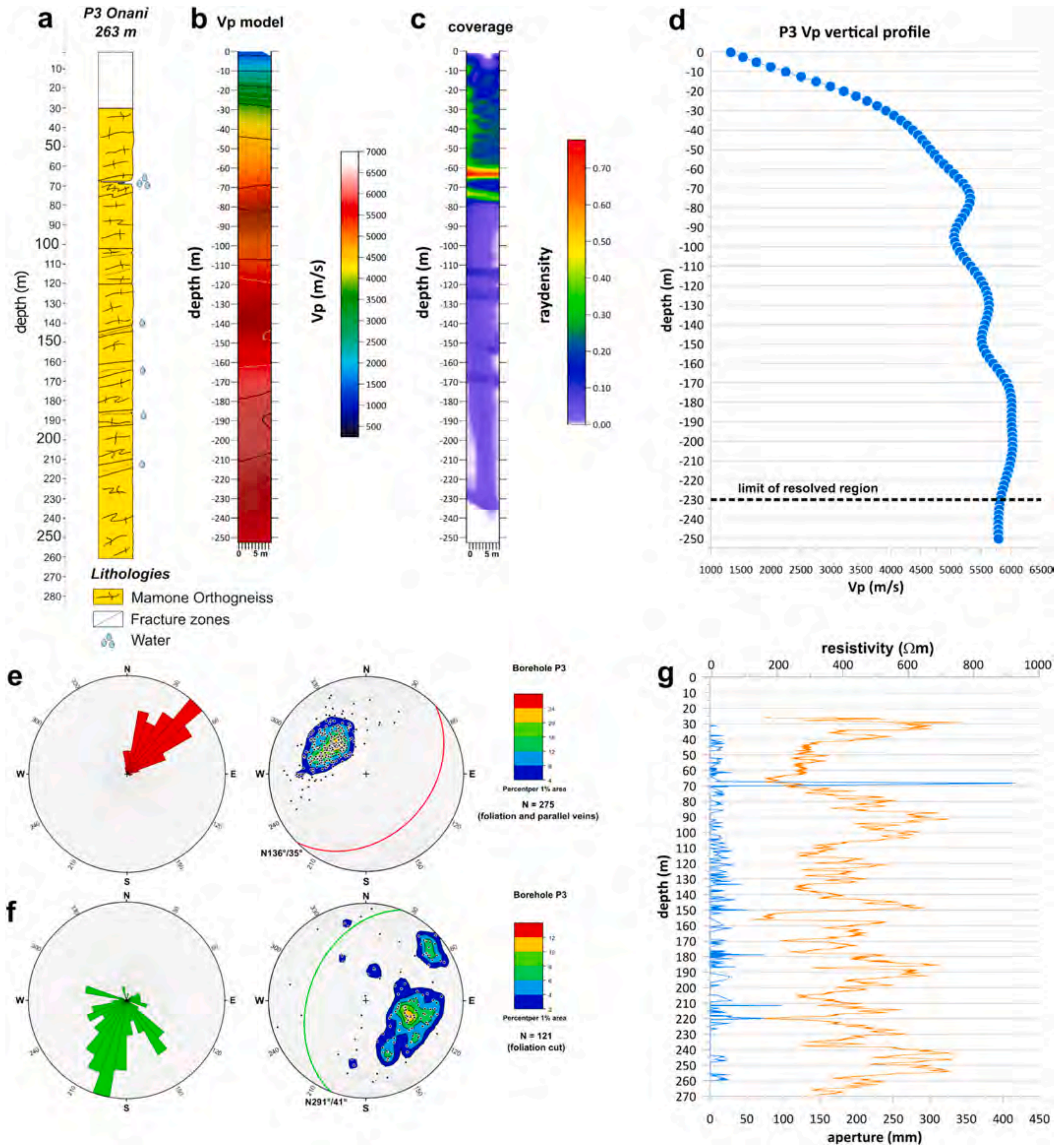

Fig. 8. Stratigraphy of borehole P3 Onanì (panel a) and comparison with results of seismic tomography. The Vp model (panel b) representative of the drilling site P3 is extracted from the 2-D tomography (Vp model shown in Fig. 7a) and shown with normalized ray coverage (panel c). The Vp vertical profile (panel d) is calculated by averaging the 2-D Vp slice shown in panel b. Structural data collected in the borehole shown as a rose diagram of fracture strike and contours of poles to planes for the main foliation and vein parallel (panel e) and for fractures that cut the main foliation (panel f). g) fracture aperture from caliper logging (blue curve) and resistivity log (orange curve) along borehole P3. (For interpretation of the references to colour in this figure legend, the reader is referred to the web version of this article.)

set of veins parallel to it (with an average dip 136°/35°). The second set has a dominant strike N191°-200°, which is related to nearly NE-striking fractures and veins that cut the the main foliation and dip 291°-041° on average.

The fracture analysis based on the integration of caliper log and borehole optical imaging (Fig. 8g) shows that fractures display almost everywhere aperture values <25 mm, with the exception of a 65–70 m deep zone with larger values (> 400 mm). This is also the depth interval at which groundwater circulation was found (Fig. 8a). The corresponding resistivity log (Fig. 8g) shows values that are generally comprised between ρ 400–600 Ωm, with a consistent drop (ρ ~200–300 Ωm at 60–80 m depth) in the region with larger fracture opening (~70 m depth). This is likely due to groundwater circulation in a fractured zone. The anomalous interval with open fractures is only a few meters shallower than the velocity reversal shown at 75–100 m depth b.g.l. in the vertical Vp profile (Fig. 8d). Taking into account the vertical spatial resolution of the 2-D tomographic model from which it was computed (~20 m, considering the node spacing; Fig. S7), we infer that the ~25–30 m-thick velocity reversal is almost resolved and may reflect the drilled fractured zone with low-resistivity. We also note that a barely visible low-Vp zone is present in the 2-D model at similar depths a few meters to the west of the borehole (Fig. 7a).

The spatial density of fractures measured in borehole P3 is low (1.82 ± 1.36 m^{-1}; Fig. S8b), and compared to that in borehole P2 it displays a lower dispersion.

This is in agreement with results of the surface and downhole seismic surveys that do not reveal important low-velocity zones below the superficial weathered zone and image very high Vp structure (> 4500–5000 m/s) starting from a depth of about 40–50 m. Moreover, the results from profile P3 *E*-W indicate that the average Vp reaches 6000–6250 m/s in a depth range of 120–200 m, thus indicating a very low degree of fracturing of the crystalline rock mass and the absence of important fault zones, consistent with the results from caliper (Fig. 8g). We discuss these findings in section 5.2.

Our results from site P3 suggest a weakly anisotropic distribution of the P-wave velocity in the first 120 m depth (that is the interval for which the maximum investigation depth reached along profile P3 N-S can be compared to that of profile P3 E-W). Fig. 9 shows the frequency Vp distributions in the shallow 120 m (excluding the weathered layer) for the two profiles. Along profile P3 E-W, the median and maximum retrieved Vp (5070 m/s and 6170 m/s, respectively) are slightly higher than those retrieved along profile P3 N-S (4960 m/s and 6070 m/s, respectively) in the same depth interval. Thus we have a median Vp difference of about 2 % and a maximum Vp difference of about 6 % along the two orthogonal directions in the first 120 m depth, with a slightly higher Vp along the E-W direction.

4.3. Results of morphostructural analysis and field survey

At a larger scale of observation over the Variscan granitoid, the analysis of satellite-derived structures has provided insights into the segmentation of major morphostructures and mapped faults (Fig. 10). As shown by their frequency distribution, DEM-derived morphostructures closely resemble those derived from satellite images in terms of trace lengths, indicating that most of them are <1.5 km long. Conversely, fault traces related to mapped structures appear to have a broader range of length, < 4 km, although their frequency diagram displays non gaussian distribution, possibly indicative of scarce fault hierarchization. The crossed-analysis of segment lengths vs. strike direction (expressed as angles) shows that segments composing morphostructures and faults are <1 km-long and are mostly representative of nearly E-W structures.

Morphostructural lineaments exhibit a predominant WSW-striking orientation and are frequently associated with E to NE-striking lineaments to form conjugated sets. We also recognized minor NNE- to NW-striking structures, which seem to cross-cut the previously described conjugated sets. Field evidence shows that both fault sets are associated with altered rocks that, especially in granitoids, can be tens of meters thick. Road cuts show that these volumes constitute fractured zones, which in the metamorphic rocks rather exhibit an anastomosing arrangement that vary in thickness from a few centimeters to a meter.

We also carried out detailed characterization of drilling sites P2 and P3 (Fig. 11) to further elucidate these morphostructural patterns. Fig. 11 illustrates a comparative morphostructural analysis using satellite images and field data in the drilling sites (see also Fig. 1b for the regional geological setting) aimed at supporting the interpretation of velocity and resistivity models. The preferred orientation of morphostructural segments was determined using FracPaQ within 0.5 Km^2 squares around the wells (yellow squares in Fig. 11). On the right-hand side, a comparison is provided with a rose diagram of the interpreted segments and systems of quartz veins (blue) and open fractures (gray) measured onsite. We observe that the length of morphostructural segments is usually <0.3 km, although the nearly E-W striking segmented morphostructural lineament crossed by the seismic line (in red in Fig. 11), is longer than 0.5 km.

In the P2 borehole site, the main WSW-striking fault is located a few tens of meters to the south of the borehole. This structure is intercepted by the seismic profile P2 and ERT survey Bt1 and spatially relates to the anomalous low-Vp/low-resistivity zone that we retrieved at x = 170–200 m along the seismic profile (Fig. 4). A direct comparison of the geophysical images of the inferred fractured zone with fractures logged into the borehole reveals that the latter, with dominant strike ranging from N040° to N070° (Fig. 5e), can be considered as representative of

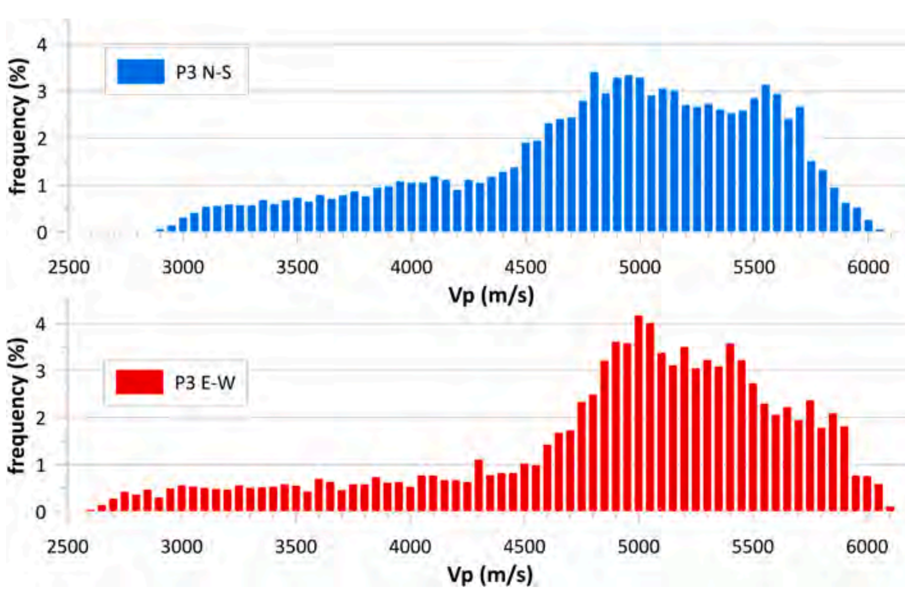

Fig. 9. Frequency histograms that compare Vp distribution in the shallow 120 m depth interval (excluding the weathered layer) from tomographic models of profiles P3 NS and P3 EW.

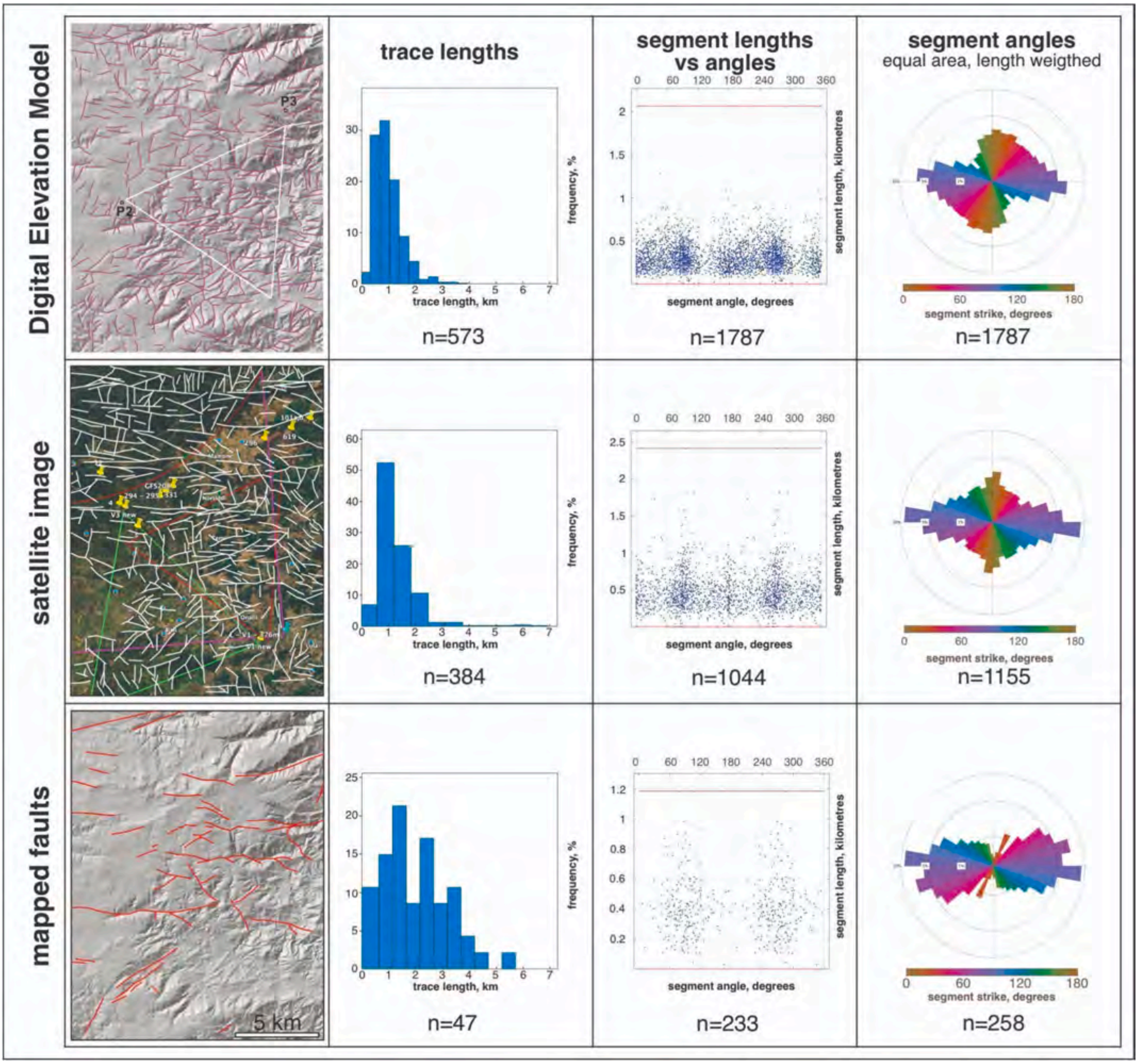

Fig. 10. Results of large-scale geometric analysis of morphostructures in the region enclosing the planned ET infrastructure. The upper and middle rows display digital elevation model (from https://www.sardegnageoportale.it/) and Google Earth Pro satellite images with superimposed lineaments elaborated with FracPaq, the frequency distribution of trace lengths, the cross-plot of trace length vs. strike and the rose diagram of azimuthal distribution. The bottom row shows geometric analysis of mapped fault traces from Fig. 1b. (For interpretation of the references to colour in this figure legend, the reader is referred to the web version of this article.)

the large-scale structural pattern revealed by the morphostructural analysis. In fact, the latter shows two main strikes N080°-090° and N020°-030°, whereas fractures collected in the field have a dominant strike N050°-060° (Fig. 11), consistent with borehole data.

In the P3 borehole site, morphostructural analysis points out two main sets of fractures striking N070°-080° and N170°-180° while field survey shows fractures and veins striking N030°-050° and N110°-120°. However, at this site, data from the borehole (Fig. 8e and f) indicate that the dominant strike of high-angle fractures cutting the main foliation is N190°-210°, consistent with surface structural data. In the northern part of the NS P3 seismic line, highlighted in red, we find an intersection of morphostructural lineaments striking WSW and NW. Additionally, we found evidence of a NW-striking lineament that is intercepted by profile P3 EW, to the west of the borehole.

5. Discussion

Our characterization of the sites P2 and P3 mainly relies on results of high-resolution active seismic surveys (Fig. 1b). By applying surface refraction tomography and downhole techniques, we were able to determine rock Vp values and image the subsurface structure down to depths ranging from approximately 90–100 (at site P2) to 230–240 m (at site P3). This information, integrated with ERT models and calibrated by well logs, enabled a reliable characterization of the rock mass in both drilling sites.

As supported by the cross-comparison with morphostructural and

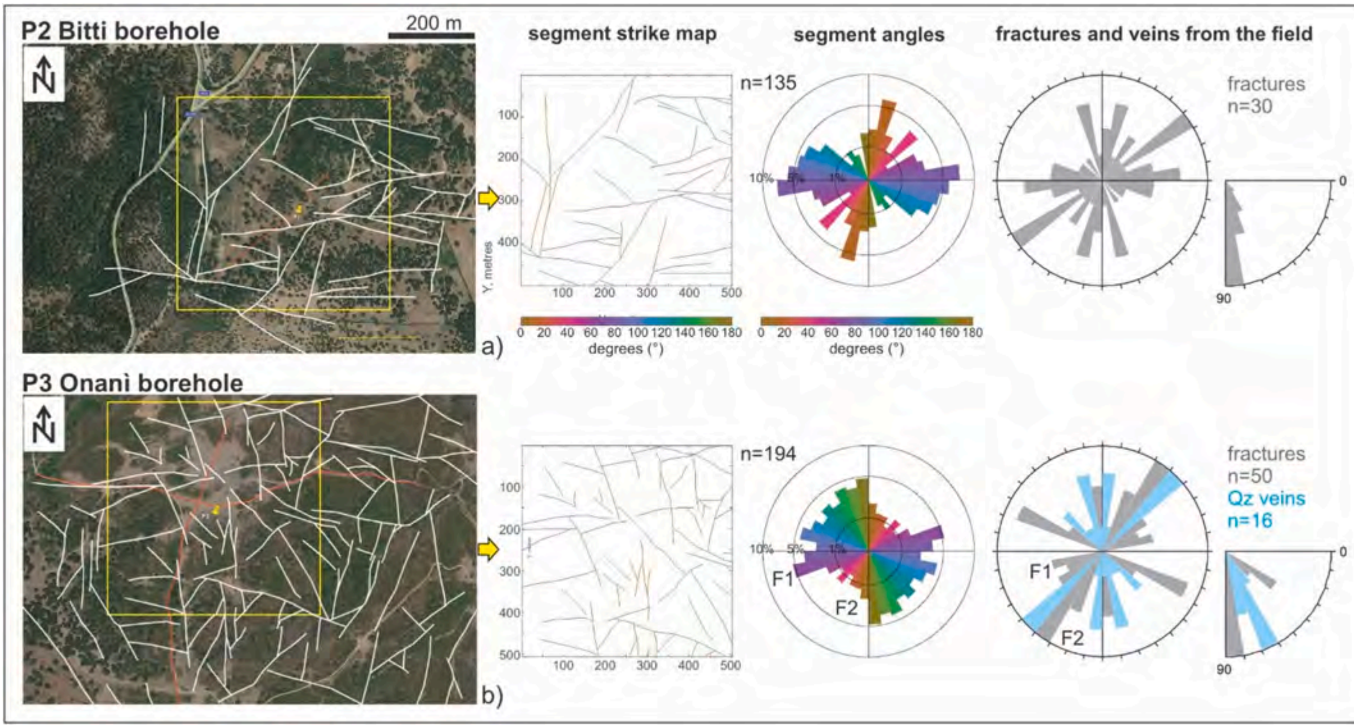

Fig. 11. Results of geometric analysis of morphostructures in the surroundings of sites P2 and P3. Red lines highlight the traces of our seismic lines. Each row displays satellite images with superimposed lineaments elaborated with FracPaq, the frequency distribution of trace lengths, the cross-plot of trace length vs. strike and the rose diagram of azimuthal distribution. (For interpretation of the references to colour in this figure legend, the reader is referred to the web version of this article.)

field-based structural analysis, we argue on the thickness of the weathered layer from the intact granitoid and orthogneiss units, and on the subsurface geometry of fractured zones, as discussed in the following.

5.1. Constraints on the P-wave velocities in granite and gneiss from literature comparison

Lithological interpretation of the P-wave velocity models described in Section 4.2 is based on comparison with literature, dealing with high-resolution geological and geophysical characterization of crystalline rocks for similar underground laboratory projects, tunnels, deep scientific drillings and nuclear waste disposal sites.

Borehole velocity measurements propaedeutic to the Bedretto (Switzerland) hydroshear and hydrofracturing underground experiments (about 1.5 km depth b.g.l.) show that weakly fractured or almost intact granites have Vp in the 5200–5500 m/s range (Ma et al., 2022; Greenwood et al., 2019). The Vp drops to 4300–4500 m/s in correspondence with a region of intense deformation characterized by frequent fault zones up to 2 m thick. Here, highly fractured granites are associated with mylonites and crackle breccias, which are structural endmembers of the ductile and brittle deformation, respectively (Cardello et al., 2024). Comparable velocity values characterize the granites and granodiorites targeted in the Grimsel (Switzerland) underground experiments (Krietsch et al., 2018). Borehole measurements integrated with underground high-resolution tomography show fractured volumes with Vp around 5200 m/s, whereas a fault-zone with a high degree of fracturing and 4–8 m thickness appears as a low-velocity zone with Vp around 4500 m/s.

In the Albala granitic test site in Spain (Martí et al., 2006), a 3D high-resolution tomography using borehole data recorded from the surface down to 500 m-depth and sonic logs shows that the velocity structure strictly correlates with the degree of fracturing. Almost intact granites below 40–60 m depth have Vp between 5500 and 6000 m/s, which can be regarded as host dry rocks (sensu Evans et al., 2005), while the top low-velocity weathered layer features Vp rapidly increasing with depth from 3000 to 4500 m/s.

Flinchum et al. (2018) in their high-resolution shallow seismic tomography investigation of the Sherman granite batholith (1.4 Ga) in the Laramide Range (Wyoming) found that the weathered layer (10–20 m-thick) has Vp in the range of 1200–2500 m/s, whereas weakly fractured and weathered granites displays Vp in the range of 4000–4900 m/s at depths greater than 20 m. These velocity values are comparable with those determined by Podugu et al. (2023) in the Western India for basement granitoids. Similarly, Benjumea et al. (2011) found that the shallow portion of Variscan granites in the Catalan Coastal Ranges (northern Spain) exhibit Vp >4500 m/s and resistivity ρ ~1000–1800 Ωm, whereas the >20 m-thick weathered layer may display Vp as low as 3000 m/s.

Summarizing, the available literature data on shallow granitoids indicate that nearly intact rock masses have high to very-high Vp in the order of 4900–6000 m/s with low vertical velocity gradient. Conversely, faulted and fractured rock masses may experience a dramatic drop in Vp, with values as low as 4300–4600 m/s. The weathered near-surface layers display Vp ranging from 1000 to 4000 m/s, with a high vertical velocity gradient. In general, these results are consistent with those derived from the inversion of both surface wave dispersion and P-wave travel times from a quarry blast, measured in the proximity of the Sos Enattos mine (Di Giovanni et al., 2020; Saccorotti et al., 2023). In both solutions, the compressional wavespeed exhibits a marked gradient at shallow depths, increasing from ~1500 m/s at the surface to about 5000 m/s at depths of about 50–70 m.

Concerning previous studies on gneiss rock mass, the work by Giese et al. (2005) based on seismic tomography investigation of the Faido access tunnel of the Gotthard Base Tunnel (Switzerland) shows that the undisturbed gneiss beyond the excavation zone displays Vp of 5800 m/s. Conversely, when intersecting important cataclastic fault zones, the Vp decreases to 3000–4500 m/s. Although computed with different methods, it is worthy to point out the reported range of P-wave velocity of 6.1–6.5 km/s for the gneiss and amphibolite rock mass drilled in the Seve Nappe (Scandinavia) by Almqvist et al. (2021).

5.2. Interpretation of results from P2 and P3 drilling sites

Taking into account constraints from literature discussed in Section 5.1, we discuss the geophysical interpretation supporting the geological reconstruction of the structures recognized in the surroundings of P2 and P3 drilling sites presented in Fig. 12.

Based on the comparison of Vp and resistivity models with borehole data, the subsurface in both P2 and P3 sites does not feature significant lithological variations. Lateral and vertical changes shown by the refraction tomography and ERT models can be instead related to variations in weathering and fracturing degree of an otherwise quite homogenous rock mass, both of which contribute to decrease seismic velocity and resistivity (e.g., Clair et al., 2015).

Regarding the Vp pattern recovered at site P2 (Fig. 4a), we recall that high Vp values near the surface (Vp around 3000 m/s just a few meters b.g.l.) are in good agreement with the patchy distribution of granites outcropping in the area. As observed in the field, this shallow level surrounds arenized and weathered granitic-derived bodies that are in contact with a stiff host rock, whose vein and fractures have been documented (Fig. 11). Overall, our geophysical and borehole data shows that this level is as thin as 15–20 m, thus including very large boulders. This shallow layer displays a step vertical gradient, with Vp increasing from 1500 to 2000 m/s near the surface to 4000 m/s at 10–15 m depth, and defines the alteration zone, consistently with the conductive weathered surface layer ($\rho < 200$–$300\ \Omega$m) imaged by ERT Bt1 (Fig. 4b). These velocity and resistivity values are similar to those of other high-resolution shallow surveys on granitoids (Flinchum et al., 2018; Martí et al., 2006; Clair et al., 2015; Section 5.1). At depths >20 m, Vp values reach ~5000 m/s indicating the occurrence of poorly fractured granitoid bodies, and are paired with high resistivity ($\rho > 1000\ \Omega$m). Higher Vp values on the southern side suggest the presence of massive and almost intact granitoids, as supported by literature data (Section 5.1). Our data points to a rapid transition from weathered granites to unweathered bedrock. Moreover, seismic velocities >5000 m/s, together with gentle vertical Vp gradient, likely reflect the general closure of fractures at depth > 20 m.

Based on literature data (Section 5.1), the low-velocity zone (Vp ~4250 m/s) in the middle of the section, which displays a 20 % drop in

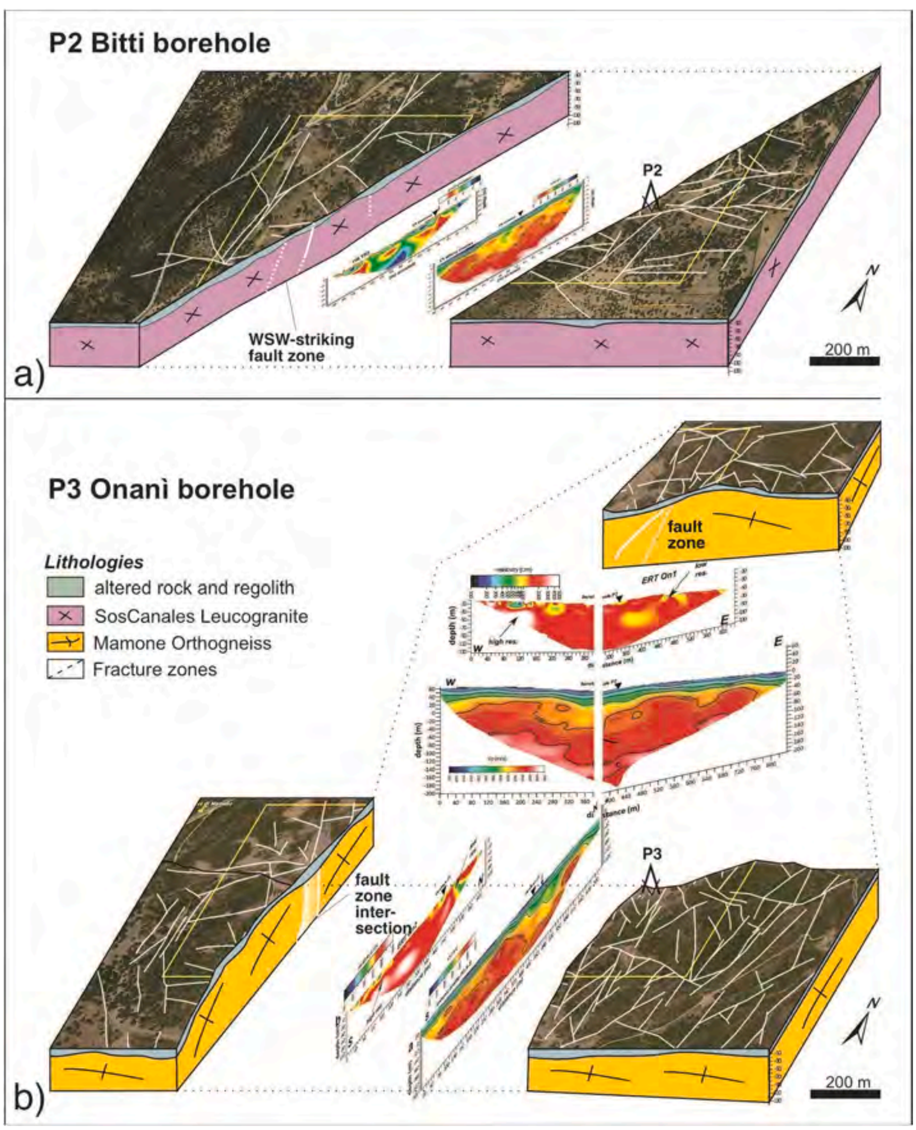

Fig. 12. Schematic interpretation models of the surface subsurface of boreholes sites P2 and P3, in perspective view. a) Interpretation of the P2 well area. b) Interpretation of the P3 well area. The figures compare the results of seismic and electrical tomography (see Figs. 4, 6, 7) with the maps of morphostructures at the surface (Fig. 11) to trace them at depth.

Vp with respect to the surrounding rock mass, can be interpreted as a sub-vertical fault-zone with a high degree of fracturing. The estimated width of the presumed fault zone, based on the size of the low-Vp anomaly and model resolution, is ~15–35 m. This interpretation is strongly supported by ERT data that coherently shows a co-located low-resistivity wedge (ρ ~350–500 Ωm).

The P2 borehole (Fig. 5a) drilled partially altered leuco-granodiorite, which in general are affected by close fractures with spatial density decreasing as a function of depth (Fig. S8a), although six thin intervals with significant fracture opening were found (Fig. 5f). The conductive/low-Vp anomaly (Fig. 4a-b) corresponds to the zone where two fault systems, that are broadly WSW-striking, are intercepted by the geophysical transect. In particular, at x = 150–160 m (Fig. 4b), we found a resistivity drop of about 150 Ωm at a depth of 40–60 m, probably related to bottom-up groundwater circulation within the fractured zone depicted in Fig. 12a. Moreover, this depth corresponds to one of the intervals with open fractures found in the borehole (Fig. 5e, aperture >1000 mm), supporting our hypothesis that these shallow fractured zones affect groundwater circulation We also observe that the high-Vp region (> 5500 m/s) in the deep part of the tomographic model displays a deflection, which might indicate that the fractured zone extends downwards, also taking into account results of resolution test (Fig. 4a; Fig. S6 and S7).

Concerning site P3 (Fig. 12b), Vp and ERT models for both P3 N-S (Fig. 6) and P3 *E*-W (Fig. 7) highlight that high-velocity and relatively shallow crystalline metamorphic rocks (Vp > 4500 m/s) are characterized by high resistivities (ρ > 1000 Ωm). Similarly, the surface weathered zone has lower resistivities (ρ < 500 Ωm). The presence of relatively homogeneous and stiff orthogneiss with very low degree of intervening fracturing (Fig. S8b) is confirmed by well logs. Borehole data (Fig. 8g) indicates that fracture opening is usually limited to <50 mm, thus generally hampering water circulation with depth. These results agree with other studies on similar rocks (Giese et al., 2005; Almqvist et al., 2021; Section 5.1).

Along profile P3 N-S, a low-Vp (3000–4000 m/s) shallow anomaly characterized by a gentle vertical velocity gradient located to the north of the borehole (at x = 430–550 m; Fig. 6a) matches a steep lateral variation shown by ERT model On2 (ρ as low as 500–800 Ωm; Fig. 6b). The edges of these shallow anomalies are located where WSW-ENE striking fault zones have been recognized both in the field and from morphostructural observation from satellite images (Fig. 11).

Seismic velocities from profile P3 E-W also show that starting from depths of about 120 m down to 230–240 m, the average Vp of the orthogneiss rock mass is as high as 6000–6250 m/s, suggesting that the degree of fracturing is extremely low, consistent with borehole data (Fig. 8g; Fig. S8b) and literature on similar rocks (Section 5.1). Moreover, we have evidence of weak seismic anisotropy, with slightly higher Vp along the E-W direction with respect to the N-S direction.

By following these observations, as depicted in Fig. 12b, we identify a possible fault zone crossed by the P3 N-S seismic profile, likely related to the intersection between the WSW- and NW-trending morphostructures, which we associate to the local decrease of seismic velocity (< 4000 m/s) and resistivity (ρ 500–800 Ωm). Additionally, we have evidence that a NW-striking fault zone is intercepted by profile P3 E-W, just to the west of the borehole, and it appears as a low-Vp region in the tomography model (Fig. 7a).

Borehole logging reports some significant groundwater content at a depth of about 70 m in borehole P3 (Fig. 8a). Based on general considerations about scaling of fault zone width as a function of fault length (e.g., Shipton et al., 2006), we suggest that only the largest fractured rock volumes in morphostructural lineaments associated with fault zones longer than 0.3–0.5 km are saturated with water, and thus capable of hosting perched aquifers. The study of the surface fracture pattern, as also recognized by a careful reconstruction of the unweathered host rock, is consistent with fracturing predicted from multiscale morphostructural and structural surveys, and thus can be used to assess the fracture geometry at depth. The very low degree of maturity of the surveyed fracture system (cf. Fig. 10 a-b) reflects in the limited extent of the fault length (< 1 km) and their scarce hierarchization (as shown by their frequency distribution: Fig. 10). We also infer that the perched aquifers correspond to the low-velocity anomalies detected along the seismic profiles (e.g. Fig. 6a and 7a). These aquifers have only been marginally intercepted in the wells (e.g. Fig. 8a), and they should also be of limited volume.

5.3. General remarks on the applied subsurface imaging strategies

Our seismic investigations revealed that the presence of a very stiff crystalline bedrock affected by predominantly closed fractures and localized fault zones is in agreement with the shallow propagation of seismic waves documented by the ray coverage of the tomographic models (Fig. S2-S7).

From a methodological point of view, we point out that, despite the use of 720 m (P3 N-S) and 835 m (P3 W-E) long recording arrays, and the inversion of P-wave first arrival times at large offsets (715–725 m from the source), refracted and turning waves propagated only within the uppermost 100 m. This represents a limitation of the applied method on high velocity crystalline rocks, since under standard geological conditions (in the absence of a very-high Vp, homogenous and shallow substratum), the depth of investigation of surface refraction tomography usually varies between 1/3 and 1/4 of the maximum observation distance of the P first arrivals. Instead, the encountered geological conditions had the effect of drastically reducing the investigation depth to approximately $^{1}/_{8}$ of the maximum observation distance. On the other hand, such a limited exploration depth provides evidence of the lack of important refractors (i.e., lithological or structural discontinuities with increasing velocities with depth) within the granitoids.

However, in the case of the seismic profile P3 E-W, we were able to significantly increase the investigation depth (about $^{1}/_{3}$ of the profile length) by integrating surface recordings with borehole data. This result documents that active seismic investigations for characterizing crystalline rock mass using 2-D refraction techniques can benefit greatly from the integration with borehole measurements. It is worth pointing out that, apart from the 1-D Vp profiles provided by downhole measurements and 2D tomography from the P3 E-W profile, the depth interval 250–400 m is devoid of geophysical information, because our seismic refraction profiles do not investigate at that depth, while no reflective faults or tectonic structures, nor other significant lithological change may be distinguished there.

Considering that most of the investigated local morphostructures in the surroundings of sites P2 and P3 display limited lateral extent (<0.3 km; Fig. 11), we suggest that any future investigation focused on the characterization of the rock mass in this region, should take into account the possibility that the largest lineaments mapped at the surface with lateral extent ranging from 0.3 to 1.5 km can host fault-related perched aquifers at depth (see Fig. 10).

Additionally, we found that on average the mechanical properties of the investigated orthogneisses (site P3) are slightly better than those retrieved in the granites of site P2, since they display a higher average Vp and lower spatial density and aperture of fractures at comparable depths.

6. Conclusions

Based on our multi-disciplinary investigations performed on Variscan granitoids at two sites of interest of the Italian site candidate for Einstein Telescope, we point out the following conclusions.

The crystalline substratum of sites P2 and P3 is characterized by homogenous and stiff rocks (granitoids and orthogneisses), partially affected by minor faults with limited extent. The transition from soil regolith or weathered granites to unweathered bedrock is located within a very thin belt, about 10–30 m thick. P-wave velocities >5000 m/s, together with low velocity gradients with depth, indicate the closure of fractures at depth > 20–30 m. P-wave velocity and electrical resistivity exhibit noticeable correlation, so that we can detect the most fractured rock volumes related to fault zones, which are characterized by lower seismic velocity and electrical resistivity with respect to the relatively intact host rock.

Borehole data indicate that those fractured zones host fault-controlled perched aquifers, and the very limited amount of water circulation is likely controlled by short and poorly interconnected fault strands, mainly WSW-striking, consistent with field and morphostructural mapping.

The only exception is represented by a prominent low-velocity zone (Vp ~4250 m/s) found immediately SW of borehole P2 (Fig. 4), which is interpreted as a steep fault zone~15–35 m-wide, with a possible downward extent of ~70 m.

Site P3 is characterized by a homogeneous and very high velocity (Vp > 6000 m/s) orthogneiss imaged at >120 m depth (Fig. 7), and displaying a subtle anisotropy in the propagation of P-waves. The absence of clear reflections suggests the lack of relevant impedance contrasts related to lithological and/or structural interfaces down to nearly 1 km depth, while borehole data indicate that the aperture of fractures being much smaller than the seismic resolution (Fig. 8g), hampers any reflectivity.More generally, our study points out that the integration of high-resolution refraction tomography with electrical resistivity tomography surveys calibrated by well logs, allows defining the main physical properties of crystalline rock masses and relating fractured zones imaged in the subsurface to faults recognized in the field. The effective investigation strategy presented in this study can be applied to similar settings characterized by crystalline basements, and provide valuable information to design future underground infrastructures.

CRediT authorship contribution statement

F. Villani: Writing – review & editing, Writing – original draft, Visualization, Validation, Supervision, Methodology, Investigation, Formal analysis, Data curation, Conceptualization. **S. Maraio:** Writing – review & editing, Writing – original draft, Visualization, Validation, Supervision, Resources, Methodology, Investigation, Formal analysis, Data curation, Conceptualization. **L. Improta:** Writing – review & editing, Writing – original draft, Validation, Supervision, Project administration, Methodology, Investigation, Funding acquisition, Data curation, Conceptualization. **P.M. De Martini:** Writing – review & editing, Writing – original draft, Validation, Supervision, Resources, Project administration, Investigation, Funding acquisition, Conceptualization. **D. Cavallaro:** Writing – review & editing, Investigation, Formal analysis. **M. Firetto Carlino:** Writing – review & editing, Investigation, Formal analysis. **C.A. Brunori:** Investigation. **V. Longo:** Resources, Methodology, Investigation, Formal analysis. **L. Casini:** Resources, Methodology, Investigation, Formal analysis. **M.C. Caradonna:** Investigation. **C. Zei:** Investigation. **S. Rapisarda:** Investigation. **G. Oggiano:** Investigation, Data curation. **C. Giunchi:** Writing – review & editing, Investigation, Funding acquisition, Conceptualization. **G. Saccorotti:** Writing – review & editing, Funding acquisition, Conceptualization. **M. Coltelli:** Writing – review & editing, Project administration, Investigation, Funding acquisition. **D. D'Urso:** Writing – review & editing, Project administration. **L. Naticchioni:** Writing – review & editing, Project administration. **F. Ricci:** Project administration. **G. Schillaci:** Project administration. **D. Cittadino:** Project administration. **M. Marsella:** Project administration. **Q. Napoleoni:** Project administration. **C. Rossini:** Project administration. **G.L. Cardello:** Writing – review & editing, Writing – original draft, Visualization, Validation, Methodology, Investigation, Data curation.

Declaration of competing interest

The authors declare that they have no known competing financial interests or personal relationships that could have appeared to influence the work reported in this paper.

Acknowledgements

This study has been conducted in the framework of the agreement between *Istituto Nazionale di Fisica Nucleare* (INFN) and *Istituto Nazionale di Geofisica e Vulcanologia* (INGV). The authors would also like to acknowledge INFN that funded this project thanks to the "*Protocollo di Intesa tra Ministero dell'Istruzione, dell'Università e della Ricerca, la Regione Autonoma della Sardegna, l'Istituto Nazionale di Fisica Nucleare e l'Università degli Studi di Sassari finalizzato a sostenere la candidatura italiana a ospitare l'infrastruttura Einstein Telescope in Sardegna e al potenziamento di Virgo*", and the University of Sassari that funded this project thanks to the "*Accordo di Programma tra la Regione Autonoma della Sardegna, l'Università degli Studi di Sassari, l'Istituto Nazionale di Fisica Nucleare, l'Istituto Nazionale di Geofisica e Vulcanologia, l'Università degli studi di Cagliari e l'IGEA S.p.a. finalizzato alla realizzazione nella Regione Autonoma della Sardegna di una infrastruttura a basso rumore sismico e antropico dedicata alla ricerca di base nell'ambito della rivelazione di onde gravitazionali, fisica della gravitazione, geofisica e sue applicazioni (progetto SARdinia-GRAVity [SAR-GRAV]). Intervento finanziato con risorse Fondo per lo Sviluppo e la Coesione (FSC) 2014–2020–Patto per lo sviluppo della Regione Sardegna*". The authors also acknowledge the *Parco Geominerario Storico e Ambientale della Sardegna* for its financial support. The authors' grateful acknowledgment also goes to the contribution of the European Cooperation in Science and Technology (COST) Action CA17137 that supported this work by an Short Term Scientific Mission (STSM) Grant and the contribution of the "*Fondi di Ateneo 2017*" of Sapienza-University of Rome. The authors also thank Andreas Rietbrock (Karlsruhe Institute of Technology) for his support and for useful discussions in the field and Stefano Bernardinetti for useful discussion about the geophysical results.

Seismic data were acquired under an agreement between INGV and *Centro di Geotecnologie* (CGT) of Siena University.

We acknowledge support of this work via a Landmark Grant Program to INGV by Halliburton Software and Services, a Halliburton Company.

We acknowledge support of the INGV "*Geologia e Geotecnologie*" Laboratory (https://www.ingv.it/monitoraggio-e-infrastrutture/laboratori/laboratorio-geologia-e-geotecnologia) for kindly providing us part of the seismic instrumentation used in this work.

We thank the editor Claire Currie and three anonymous reviewers that provided insightful comments that have improved the initial version of the manuscript.

Appendix A. Supplementary data

Supplementary data to this article can be found online at https://doi.org/10.1016/j.tecto.2025.230830.

Data availability

Data will be made available on request.

References

Ahmed, K.A., Dell, S., Schwarz, B., Gajewski, D., Ettrich, N., 2019. 3-D seismic imaging in crystalline rock environment: an approach based on diffraction focusing. J. Appl. Geophys. 165, 49–59. https://doi.org/10.1016/j.jappgeo.2019.04.003.

Aizebeokhai, A.P., Ogungbade, O., Oyeyemi, K.D., 2018. Geoelectrical resistivity data set for characterising crystalline basement aquifers in Basiri, Ado-Ekiti, southwestern Nigeria. Data Brief 19, 810–816. https://doi.org/10.1016/j.dib.2018.05.091.

Allmendinger, R.W., Cardozo, N., Fisher, D., 2012. Structural Geology Algorithms: Vectors and Tensors in Structural Geology. Cambridge University Press. ISBN 978-1-107-01200-4.

Allocca, A., Berbellini, A., Boschi, L., Calloni, E., Cardello, G.L., Cardini, A., Trozzo, L., 2021. Seismic glitchiness at Sos Enattos site: impact on intermediate black hole binaries detection efficiency. Eur. Phys. J. Plus 136 (5), 511.
Almqvist, B.S., Cyprych, D., Piazolo, S., 2021. Seismic anisotropy of mid crustal orogenic nappes and their bounding structures: an example from the Middle Allochthon (Seve Nappe) of the Central Scandinavian Caledonides. Tectonophysics 819, 229045.
Aning, A., Sarfo, C., Mainoo, P., Noye, R., 2019. 2D Electrical Resistivity Imaging for Delineation of Crystalline Basement Aquifer in Northern Ghana. J. Geosci. Environ. Protect. 7, 102–115. https://doi.org/10.4236/gep.2019.712007.
Belle, P., Lachassagne, P., Mathieu, F., Barbet, C., Brisset, N., Gourry, J.C., 2019. Characterization and location of the laminated layer within hard rock weathering profiles from electrical resistivity tomography: implications for water well siting. Geol. Soc. Lond. Spec. Publ. 479 (1), 187–205. https://doi.org/10.1144/SP479.7.
Benjumea, B., Macau, A., Gabàs, A., Bellmunt, F., Figueras, S., Cirés, J., 2011. Integrated geophysical profiles and H/V microtremor measurements for subsoil characterization. Near Surf. Geophys. 9, 413–425. https://doi.org/10.3997/1873-0604.2011021.
Bernardinetti, S., Pieruccioni, D., Mugnaioli, E., Talarico, F.M., Trotta, M., Harroud, A., Tufarolo, E., 2018. A pilot study to test the reliability of the ERT method in the identification of mixed sulphides bearing dykes: the example of Sidi Flah mine (Anti-Atlas, Morocco). Ore Geol. Rev. 101, 819–838. https://doi.org/10.1016/j.oregeorev.2018.08.028.
Bharti, A.K., Singh, S.K., Pal, S.K., Singh, K.K.K., Prakash, A., Bhattacharjee, R., et al., 2023. Electrical resistivity tomography technique coupled with numerical modelling: a case study for stability analysis. Geophys. Prospect. 71, 1368–1384. https://doi.org/10.1111/1365-2478.13382.
Bruno, P.P.G., Maraio, S., Festa, G., 2017. The shallow structure of Solfatara Volcano, Italy, revealed by dense, wide-aperture seismic profiling. Sci. Rep. 7 (1), 17386.
Bruno, P.P.G., Villani, F., Improta, L., 2022. High-resolution seismic imaging of fault-controlled basins: A case study from the 2009 Mw 6.1 central Italy earthquake. Tectonics 41 (4), e2022TC007207.
Buske, S., Bellefleur, G., Malehmir, A., 2016. Introduction to special issue on “hard rock seismic imaging”. Geophys. Prospect. 63 (4). https://doi.org/10.1111/1365-2478.12257.
Cardello, G.L., Bernasconi, S.M., Fellin, M.G., Rahn, M., Rosskopf, R., Maden, C., Mancktelow, N.S., 2024. Carbonate deformation through the brittle-ductile transition: the case of the SW Helvetic nappes, Switzerland. J. Struct. Geol. 181, 105083.
Carmignani, L., Carosi, R., Di Pisa, A., Gattiglio, M., Musumeci, G., Oggiano, G., Carlo Pertusati, P., 1994. The hercynian chain in Sardinia (Italy). Geodin. Acta 7 (1), 31–47.
Carmignani, L., Oggiano, G., Funedda, A., Conti, P., Pasci, S., 2015. The geological map of Sardinia (Italy) at 1:250,000 scale. J. Maps. https://doi.org/10.1080/17445647.2015.1084544.
Carosi, R., Petroccia, A., Iaccarino, S., Simonetti, M., Langone, A., Montomoli, C., 2020. Kinematics and timing Constraints in a Transpressive Tectonic Regime: the example of the Posada-Asinara Shear Zone (NE Sardinia, Italy). Geosciences 10 (8), 288. https://doi.org/10.3390/geosciences10080288.
Casini, L., Cuccuru, S., Maino, M., Oggiano, G., Tiepolo, M., 2012. Emplacement of the Arzachena Pluton (Corsica–Sardinia Batholith) and the geodynamics of incoming Pangaea. Tectonophysics 544-545, 31–49.
Casini, L., Cuccuru, S., Puccini, A., Oggiano, G., Rossi, P., 2015a. Evolution of the Corsica–Sardinia Batholith and late-orogenic shearing of the Variscides. Tectonophysics 646, 65–78. https://doi.org/10.1016/j.tecto.2015.01.017.
Casini, L., Cuccuru, S., Maino, M., Oggiano, G., Puccini, A., Rossi, P., 2015b. Structural map of Variscan northern Sardinia (Italy). J. Maps 1–10.
Clair, J.St., Moon, S., Holbrook, W.S., Perron, J.T., Riebe, C.S., Martel, S.J., Carr, B., Harman, C., Singha, K., Richter, D.B., 2015. Geophysical imaging reveals topographic stress control of bedrock weathering. Science 350 (6260), 534–538. https://doi.org/10.1126/science.aab2210.
Constable, S.C., Parker, R.L., Constable, C.G., 1987. Occam’s inversion: A practical algorithm for generating smooth models from electromagnetic sounding data. Geophysics 52 (3), 289–300.
Dahlin, T., 1996. 2D resistivity surveying for environmental and engineering applications. First break 14 (7).
Di Giovanni, M., Giunchi, C., Saccorotti, G., Berbellini, A., Boschi, L., Olivieri, M., De Rosa, R., Naticchioni, L., Oggiano, G., Carpinelli, M., D’Urso, D., Cuccuru, S., Sipala, V., Calloni, E., Di Fiore, L., Grado, A., Migoni, C., Cardini, A., Paoletti, P., Fiori, I., An Harms, J., Majorana, E., Rapagnani, P., Ricci, F., Punturo, M., 2020. A Seismological Study of the Sos Enattos Area—the Sardinia Candidate Site for the Einstein Telescope. Seismol. Res. Lett. 92 (1), 352–364. https://doi.org/10.1785/0220200186.
Di Giovanni, M., Koley, S., Ensing, J.X., Andric, T., Harms, J., D’Urso, D., et al., 2023. Temporal variations of the ambient seismic field at the Sardinia candidate site of the Einstein Telescope. Geophys. J. Int. 234 (3), 1943–1964. https://doi.org/10.1093/gji/ggad178.
Di Vincenzo, G., Ghezzo, C., Tonarini, S., 1994. Geochemistry and Rb/Sr geochronology of the Hercynian peraluminous Sos Canales pluton (Central Sardinia, Italy). Compt. Rend. l’Acad. Sci. Paris 319 (7), 783–790.
Di Vincenzo, G., Carosi, R., Palmeri, R., 2004. The relationship between tectono-metamorphic evolution and argon isotope records in white mica: constraints from in situ 40Ar–39Ar laser analysis of the Variscan basement of Sardinia. J. Petrol. 45 (5), 1013–1043.
Doetsch, J., Krietsch, H., Schmelzbach, C., Jalali, M., Gischig, V., Villiger, L., Amann, F., Maurer, H., 2020. Characterizing a decametre-scale granitic reservoir using ground-penetrating radar and seismic methods. Solid Earth 11, 1441–1455. https://doi.org/10.5194/se-11-1441-2020.
Duz, B.G., Moreira, C.A., Casagrande, M.F.S., Helene, L.P.I., 2023. Mapping the integrity of rock mass with GPR: case study in decommissioning mining. SN Appl. Sci. 5, 231. https://doi.org/10.1007/s42452-023-05422-8.
Elger, J., Berndt, C., Kästner, F., Pierdominici, S., Kück, J., Almqvist, B.S., Lorenz, H., 2021. Core-log-seismic integration in metamorphic rocks and its implication for the regional geology: a case study for the ICDP drilling project COSC-1, Sweden. Geochem. Geophys. Geosyst. 22 (3), e2020GC009376.
ET design report update 2020, 2020. ET Steering Committee Editorial Team, 247 pp. https://apps.et-gw.eu/tds/?r=18715.
Evans, K.F., Moriya, H., Niitsuma, H., Jones, R.H., Phillips, W.S., Genter, A., Baria, R., 2005. Microseismicity and permeability enhancement of hydrogeologic structures during massive fluid injections into granite at 3 km depth at the Soultz HDR site. Geophys. J. Int. 160 (1), 388–412.
Everett, M.E., 2013. Near-surface applied geophysics. Cambridge University Press.
Ferrara, G., Ricci, C.A., Rita, F., 1978. Isotopic ages and tectono-metamorphic history of the metamorphic basement of North-Eastern Sardinia. Contrib. Mineral. Petrol. 68, 99–106.
Flinchum, B.A., Steven Holbrook, W., Rempe, D., Moon, S., Riebe, C.S., Carr, B.J., et al., 2018. Critical zone structure under a granite ridge inferred from drilling and three-dimensional seismic refraction data. J. Geophys. Res. Earth 123, 1317–1343. https://doi.org/10.1029/2017JF004280.
Giese, R., Klose, C., Borm, G., 2005. In situ seismic investigations of fault zones in the Leventina Gneiss complex of the Swiss Central Alps. In: Harvey, P.K., Brewer, T.S., Pezard, P.A., Petrov, V.A. (Eds.), Petrophysical Properties of Crystalline Rocks, 240. Geological Society, London, pp. 15–24. Special Publications.
Giocoli, A., Stabile, T.A., Adurno, I., Perrone, A., Gallipoli, M.R., Gueguen, E., Piscitelli, S., 2015. Geological and geophysical characterization of the southeastern side of the High Agri Valley (southern Apennines, Italy). Nat. Hazards Earth Syst. Sci. 15 (2), 315–323.
Greenwood, A., Caspari, E., Egli, D., Baron, L., Zahner, T., Hunziker, J., Holliger, K., 2019. Characterization and imaging of a hydrothermally active near-vertical fault zone in crystalline rocks based on hydrophone VSP data. Tectonophysics 750, 153–176.
Harms, J., Naticchioni, L., Calloni, E., et al., 2022. A lower limit for Newtonian-noise models of the Einstein Telescope. Eur. Phys. J. Plus 137, 687. https://doi.org/10.1140/epjp/s13360-022-02851-z.
Healy, D., Rizzo, R.E., Cornwell, D.G., Farrell, N.J., Watkins, H., Timms, N.E., Smith, M., 2017. FracPaQ: a MATLAB™ toolbox for the quantification of fracture patterns. J. Struct. Geol. 95, 1–16.
Hedin, P., Almqvist, B., Berthet, T., Juhlin, C., Buske, S., Simon, H., Giese, R., Krauss, F., Rosberg, J.-E., Alm, P.-G., 2016. 3D reflection seismic imaging at the 2.5km deep COSC-1 scientific borehole, central Scandinavian Caledonides. Tectonophysics 689, 40–55. https://doi.org/10.1016/j.tecto.2015.12.013.
Herrero, A., Zollo, A., Virieux, J., 1999. 2D Non linear first arrival time inversion applied to Mt. Vesuvius active seismic data (TomoVes96). In: Eur. Geophys. Soc., XXIV, General Assembly, 19–23 April, 1999, The Hague, The Netherlands.
Improta, L., Zollo, A., Herrero, A., Frattini, R., Virieux, J., Dell’Aversana, P., 2002. Seismic imaging of complex structures by non-linear traveltime inversion of dense wide-angle data: Application to a thrust belt. Geophys. J. Int. 151, 264–278. https://doi.org/10.1046/j.1365-246X.2002.01768.x.
Improta, L., Bruno, P.P., 2007. Combining seismic reflection with multifold wide-aperture profiling: An effective strategy for high-resolution shallow imaging of active faults. Geophys. Res. Lett. 34 (20).
Improta, L., Ferranti, L., De Martini, P.M., Piscitelli, S., Bruno, P.P., Burrato, P., Civico, R., Giocoli, A., Iorio, M., D’Addezio, G., Maschio, L., 2010. Detecting young, slow-slipping active faults by geologic and multidisciplinary high-resolution geophysical investigations: a case study from the Apennine seismic belt, Italy. J. Geophys. Res. 115, B11307. https://doi.org/10.1029/2010JB000871.
Kim, J.S., Moon, W.H., Lodha, G., Serzu, M., Soonawala, N., 1994. Imaging of reflection seismic energy for mapping shallow fracture zones in crystalline rocks. Geophysics 59 (5), 753–765. https://doi.org/10.1190/1.1443633.
Krietsch, H., Doetsch, J., Dutler, N., Jalali, M., Gischig, V., Loew, S., Amann, F., 2018. Comprehensive geological dataset describing a crystalline rock mass for hydraulic stimulation experiments. Sci. data 5 (1), 1–12.
Kuang, X., Zhu, X., Ning, F., Li, W., Zheng, Q., Li, B., Zhou, D., 2022. Aeromagnetic-Imaged Basement Fault Structure of the Eastern Tarim Basin and its Tectonic Implication. Front. Earth Sci. 9, 825498. https://doi.org/10.3389/feart.2021.825498.
Lecomte, I., Gyoistdal, H., Dahle, A., Pedersen, O.C., 2000. Improving modelling and inversion in refraction seismics with a first-order eikonal solver. Geophys. Prospect. 48 (3). https://doi.org/10.1046/j.1365-2478.2000.00201.x.
Loke, M.H., Barker, R.D., 1995. Least-squares deconvolution of apparent resistivity pseudosections. Geophysics 60 (6), 1682–1690.
Loke, M.H., Dahlin, T., 2002. A comparison of the Gauss–Newton and quasi-Newton methods in resistivity imaging inversion. J. Appl. Geophys. 49 (3), 149–162.
Loke, M.H., 2010. Res2Dinv ver. 3.59 for Windows XP/Vista/7 2010. Rapid 2-D Resistivity & IP Inversion Using the Least-Squares Method. Geoelectrical Imaging 2D & 3D Geotomo Software 2010, Malaysia.
Longo, V., Cardello, G.L., 2021. Prospezioni geoelettriche nel sito sardo candidato ad ospitare l’Einstein Telescope. Relazione Geofisica, Settembre 2021 (resp. D. D’urso, G. Oggiano). Università degli Studi di Sassari, Dipartimento di Chimica e Farmacia.
Ma, L., Xu, T., Ai, Y., Yang, J., Yang, Y., Fan, E., Dong, W., 2022. Hot lithosphere beneath the northeastern North China Craton detected by ambient noise tomography. Tectonophysics 839, 229551.

Maraio, S., Villani, F., Bruno, P.P., Sapia, V., Improta, L., 2023. Active fault detection and characterization by ultrashallow seismic imaging: a case study from the 2016 Mw 6.5 Central Italy earthquake. Tectonophysics. https://doi.org/10.1016/j.tecto.2023.229733.
Martí, D., Carbonell, R., Escuder-Viruete, J., Pérez-Estaún, A., 2006. Characterization of a fractured granitic pluton: P- and S-waves seismic tomography and uncertainty analysis. Tectonophysics 422, 99–114. https://doi.org/10.1016/j.tecto.2006.05.012.
Meju, M.A., 2005. Non-invasive characterization of fractured crystalline rocks using a combined multicomponent transient electromagnetic, resistivity and seismic approach, vol. 240. Geological Society, London, pp. 195–206. https://doi.org/10.1144/GSL.SP.2005.240.01.15. Special Publications.
Meletti, C., Camassi, R., Castelli, V., 2020. A Reappraisal of the Seismicity of Sardinia, Italy. Seismol. Res. Lett. 92 (2A), 1148–1158. https://doi.org/10.1785/0220200255.
Moon, W.M., Kim, J.S., Lodha, G., Serzu, M., Soonawala, N., 1993. Application of high resolution seismic reflection techniques for fracture mapping in crystalline rocks. Eng. Geol. 34 (3–4), 261–280. https://doi.org/10.1016/0013-7952(93)90093-R.
Nasuti, A., Roberts, D., Dumais, M.A., Ofstad, F., Hyvönen, E., Stampolidis, A., 2015. New high-resolution aeromagnetic and radiometric surveys in Finnmark and North Troms: linking anomaly patterns to bedrock geology and structure. Nor. J. Geol. 95 (3), 4. https://doi.org/10.17850/njg95-3-10.
Naticchioni, L., Perciballi, M., Ricci, F., Coccia, E., Malvezzi, V., Acernese, F., Loddo, G., 2014. Microseismic studies of an underground site for a new interferometric gravitational wave detector. Class. Quant. Grav. 31 (10), 105016.
Naticchioni, L., Cardello, L., Cittadino, D., D'Urso, D., Di Giovanni, M., Giunchi, C., Marsella, M., Napoleoni, Q., Oggiano, G., Perciballi, M., Rapagnani, P., Ricci, F., Rossini, C., Saccorotti, G., Schillaci, G., 2021. In ET –Site Studies and Characterization Workshop –Nuoro, Nov. 8-11, 2021.
Naticchioni, L., Allocca, A., Boschi, V., Cadeddu, M., Cadoni, M., Calloni, E., Tuveri, M., 2024. Characterizing the Sardinia candidate site for the Einstein Telescope. In: POS PROCEEDINGS OF SCIENCE, XVIII International Conference on Topics in Astroparticle and Underground Physics (TAUP2023) - Gravitational Waves, p. 441. https://pos.sissa.it/441/110. 10.22323/1.441.0110.
Nguyen, F., Garambois, S., Jongmans, D., Pirard, E., Loke, M.H., 2005. Image processing of 2D resistivity data for imaging faults. J. Appl. Geophys. 57, 260–277. https://doi.org/10.1016/j.jappgeo.2005.02.001.
Oggiano, G., Di Pisa, A., 1992. Geologia della catena ercinica in Sardegna-Zona Assiale. In: Carmignani, L., et al. (Eds.), Struttura della Catena Ercinica in Sardegna: Guida alla Escursione sul basamento paleozoico. Centrooffset, Siena, pp. 147–177.
Ortner, H., Reiter, F., Acs, P., 2002. Easy handling of tectonic data: the programs TectonicVB for Mac and TectonicsFP for Windows™. Comput. Geosci. 28 (10), 1193–1200.
Park, S.K., Roberts, J.J., 2003. Conductivity structure of the San Andreas fault, Parkfield, revisited. Geophys. Res. Lett. 30 (16), 1842. https://doi.org/10.1029/2003GL017689.
Park, C.B., Miller, R.D., Xia, J., 1999. Multichannel analysis of surface waves. Geophysics 64, 800–808. https://doi.org/10.1190/1.1444590.
Place, J., Malehmir, A., 2016. Using supervirtual first arrivals in controlled-source hardrock seismic imaging—well worth the effort. Geophys. J. Int. 206 (1), 716–730. https://doi.org/10.1093/gji/ggw176.
Podugu, N., Goswami, D., Akkiraju, V.V., Roy, S., 2023. In-situ physical and elastic properties of Archaean basement granitoids in the Koyna seismogenic zone, western India from 3 km downhole geophysical well logs: Implications for water percolation at depth. Tectonophysics 848, 229725.
Podvin, P., Lecomte, I., 1991. Finite difference computation of traveltimes in very contrasted velocity models: a massively parallel approach and its associated tools. Geophys. J. Int 105 (1), 271–284.
Punturo, M., et al., 2010. The Einstein Telescope: a third-generation gravitational wave observatory. Class. Quant. Grav. 27, 194002. https://doi.org/10.1088/0264-9381/27/19/194002.
Ravaut, C., Operto, S., Improta, L., Virieux, J., Herrero, A., Dell'Aversana, P., 2004. Multiscale imaging of complex structures from multifold wide aperture seismic data by frequency-domain full-waveform tomography: application to a thrust belt. Geophys. J. Int. 159, 1032–1056.
Saccorotti, G., Giunchi, C., D'Ambrosio, M., Gaviano, S., Naticchioni, L., D'Urso, D., Trozzo, L., 2023. Array analysis of seismic noise at the Sos Enattos mine, the Italian candidate site for the Einstein Telescope. Eur. Phys. J. Plus 138 (9), 793.
Sahoo, S.D., Pal, S.K., Vikash, V., et al., 2024. Quantifying environmental impact of unplanned mining through integrated non-invasive geophysical methods: a case study from Jharia coalfield, India. Environ. Earth Sci. 83, 411. https://doi.org/10.1007/s12665-024-11719-7.
Sahoo, S.D., Vikash, V., Pal, S.K., et al., 2025. Combined magnetic and surface wave analysis of a coal fire affected site at Barora, Jharia Coalfield, India: evidence of subsurface cavity and low velocity layers. Acta Geophys. 73, 1393–1415. https://doi.org/10.1007/s11600-024-01422-3.
Schmelzbach, C., Horstmeyer, H., Juhlin, C., 2007. Shallow 3D seismic-reflection imaging of fracture zones in crystalline rock. Geophysics 72, B149–B160. https://doi.org/10.1190/1.2787336.
Schuster, G.T., Quintus-Bosz, A., 1993. Wavepath eikonal traveltime inversion: Theory. Geophysics 58 (9), 1314–1323.
Servizio Geologico d''Italia, 1962. Carta Geologica d'Italia alla scala 1:100.000, F. 194 Ozieri. ISPRA, Roma. http://sgi.isprambiente.it/geologia100k/mostra_foglio.aspx?numero_foglio=194.
Shah, A.K., Crain, K., 2018. Aeromagnetic data reveal potential seismogenic basement faults in the induced seismicity setting of Oklahoma. Geophys. Res. Lett. 45, 5948–5958. https://doi.org/10.1029/2018GL077768.
Shipton, Z.K., Soden, A.M., Kirkpatrick, J.D., Bright, A.M., Lunn, R.J., 2006. How thick is a fault? Fault displacement-thickness scaling revisited. In: Abercrombie, R., McGarr, A., Di Toro, G., Kanamori, H. (Eds.), Earthquakes: Radiated Energy and the Physics of Faulting. https://doi.org/10.1029/170GM19.
Silvester, P.P., Ferrari, R.L., 1996. *Finite elements for electrical engineers*. Cambridge university press.
Siren, T., Hakala, M., Valli, J., Kantia, P., Hudson, J.A., Johansson, E., 2015. In situ strength and failure mechanisms of migmatitic gneiss and pegmatitic granite at the nuclear waste disposal site in Olkiluoto, Western Finland. Int. J. Rock Mech. Min. Sci. 79, 135–148.
Srivastava, S., Kumar, R., Pal, S.K., et al., 2024. Mapping of old coal mine galleries near railway track using electrical resistivity tomography and magnetic approaches in Tundu, Jogidih Colliery, Jharia Coalfield, India. J. Earth Syst. Sci. 133, 57. https://doi.org/10.1007/s12040-023-02253-4.
Unsworth, M.J., Malin, P.E., Egbert, G.D., Booker, J.R., 1997. Internal structure of the San Andreas fault zone at Parkfield. Calif. Geol. 25, 359–362.
Villani, F., Tulliani, V., Sapia, V., Fierro, E., Civico, R., Pantosti, D., 2015. Shallow subsurface imaging of the Piano di Pezza active normal fault (Central Italy) by high resolution refraction and electrical resistivity tomography coupled with time-domain electromagnetic data. Geophys. J. Int. 203 (3), 1482–1494. https://doi.org/10.1093/gji/ggv399.
Villani, F., Maraio, S., Bruno, P.P., Improta, L., Wood, K., Pucci, S., Civico, R., Sapia, V., De Martini, P.M., Brunori, C.A., Doglioni, C., Pantosti, D., 2021. High-resolution seismic profiling in the hanging wall of the southern fault section ruptured during the 2016 Mw 6.5 Central Italy earthquake. Tectonics 40 (9), e2021TC006786. https://doi.org/10.1029/2021TC006786.
Watanabe, T., Matsuoka, T., Ashida, Y., 1999. Seismic traveltime tomography using Fresnel volume approach. In: SEG Technical Program Expanded Abstracts 1999. Society of Exploration Geophysicists, pp. 1402–1405.
Wenning, Q.C., Berthet, T., Ask, M., Zappone, A., Rosberg, J.E., Almqvist, B.S., 2017. Image log analysis of in situ stress orientation, breakout growth, and natural geologic structures to 2.5 km depth in central Scandinavian Caledonides: results from the COSC-1 borehole. J. Geophys. Res. Solid Earth 122 (5), 3999–4019.
Yadav, A., Kumar, T., Tripathi, A., et al., 2024. Combined electrical resistivity tomography and high-resolution shallow seismic analysis for coal exploration in Talcher Coalfield, India. Acta Geophys. 72, 4263–4293. https://doi.org/10.1007/s11600-024-01349-9.
Zhang, Y., Li, Y.E., Kua, T., 2020. A modified seismic reflection approach for engineering geology investigation in fractured rock zones. Eng. Geol. 270. https://doi.org/10.1016/j.enggeo.2020.105592.